Monthly Notices
of the
ROYAL ASTRONOMICAL SOCIETY

MNRAS **469,** 2913–2932 (2017)
Advance Access publication 2017 April 21

doi:10.1093/mnras/stx957

The H α luminosity-dependent clustering of star-forming galaxies from $z \sim 0.8$ to $\sim$2.2 with HiZELS

R. K. Cochrane,[1⋆] P. N. Best,[1] D. Sobral,[2,3] I. Smail,[4] D. A. Wake,[5] J. P. Stott[2,6] and J. E. Geach[7]

[1]*SUPA, Institute for Astronomy, Royal Observatory, Edinburgh EH9 3HJ, UK*
[2]*Department of Physics, Lancaster University, Lancaster LA1 4YB, UK*
[3]*Leiden Observatory, Leiden University, PO Box 9513, NL-2300 RA Leiden, The Netherlands*
[4]*Department of Physics, Centre for Extragalactic Astronomy, Durham University, South Road, Durham DH1 3LE, UK*
[5]*Department of Physical Sciences, The Open University, Milton Keynes MK7 6AA, UK*
[6]*Subdepartment of Astrophysics, Department of Physics, University of Oxford, Denys Wilkinson Building, Keble Road, Oxford OX1 3RH, UK*
[7]*Centre for Astrophysics Research, Science & Technology Research Institute, University of Hertfordshire, Hatfield AL10 9AB, UK*

Accepted 2017 April 19. Received 2017 April 18; in original form 2016 December 20

ABSTRACT

We present clustering analyses of identically selected star-forming galaxies in three narrow redshift slices (at $z = 0.8$, 1.47 and 2.23), from the High-Redshift(Z) Emission Line Survey (HiZELS), a deep, near-infrared narrow-band survey. The HiZELS samples span the peak in the cosmic star formation rate density, identifying typical star-forming galaxies at each epoch. Narrow-band samples have well-defined redshift distributions and are therefore ideal for clustering analyses. We quantify the clustering of the three samples, and of H α luminosity-selected subsamples, initially using simple power-law fits to the two-point correlation function. We extend this work to link the evolution of star-forming galaxies and their host dark matter haloes over cosmic time using sophisticated dark matter halo models. We find that the clustering strength, r_0, and the bias of galaxy populations relative to the clustering of dark matter increase linearly with H α luminosity (and, by implication, star formation rate) at all three redshifts, as do the host dark matter halo masses of the HiZELS galaxies. The typical galaxies in our samples are star-forming centrals, residing in haloes of mass $M_{\rm halo} \sim$ a few times $10^{12}\,{\rm M}_{\odot}$. We find a remarkably tight redshift-independent relation between the H α luminosity scaled by the characteristic luminosity, $L_{{\rm H}\alpha}/L^{*}_{{\rm H}\alpha}(z)$, and the minimum host dark matter halo mass of central galaxies. This reveals that the dark matter halo environment is a strong driver of galaxy star formation rate and therefore of the evolution of the star formation rate density in the Universe.

Key words: galaxies: evolution – galaxies: haloes – galaxies: high-redshift – large-scale structure of Universe.

1 INTRODUCTION

The galaxies we observe exist in a wide range of environments, from rich clusters to underdense void regions. They are thought to trace an underlying distribution of dark matter, with more highly clustered galaxies occupying massive dark matter overdensities (Zwicky 1933; Peebles 1982). This is commonly explained via the paradigm of hierarchical growth: weak density fluctuations in an expanding, homogeneous Universe are amplified by gravitational instabilities, with smaller structures forming first. Galaxies form due to the collapse of baryonic matter under the gravity of dark matter haloes (White & Frenk 1991), with the progenitors of the most massive clusters starting to form earliest. Dark matter haloes assemble via successive mergers and accretion of small haloes, which naturally leads to the formation of galaxy groups and clusters, with a single dark matter halo capable of hosting many galaxies.

Whilst the observed 'cosmic web' spatial distribution of dark matter in the Λ cold dark matter paradigm can be successfully modelled using *N*-body simulations (Davis et al. 1985) as advanced as the Millennium simulation (Springel et al. 2005), resolution is limited and the evolution of galaxies within this web is harder to model. This complexity reflects the additional baryonic processes present: we must consider not only the underlying distribution of dark matter but also the non-linear physics of galaxy formation and evolution. Key processes such as gas cooling, star formation and

⋆ E-mail: rcoch@roe.ac.uk

the physics of feedback due to star formation and black hole accretion all act on different time-scales with different galaxy mass and environment dependences. The latest generation of hydrodynamical simulations such as Illustris (Vogelsberger et al. 2014) and EAGLE (Crain et al. 2015; Schaye et al. 2015) and semi-analytic models (e.g. Baugh 2006) currently do fairly well in modelling such processes, broadly reproducing key observed relations such as galaxy luminosity and stellar mass functions, and the bimodal galaxy colour distribution, but a wealth of observational data is required to fine-tune parameters.

Many details of the environmental drivers of galaxy evolution, and how they relate to galaxy mass, remain poorly understood. It has long been known that at low redshifts, galaxies in rich clusters are preferentially passive ellipticals (Oemler 1977; Dressler 1980), whereas field galaxies tend to be star-forming and disc-like, with increasing star formation rates (SFR) and star-forming fractions further from cluster centres (Lewis et al. 2002; Gomez et al. 2003). High-mass galaxies are also far less likely to be star-forming than their low-mass counterparts (Baldry et al. 2006). Despite these well-established observational trends, the effects of mass and environment have remained hard to distinguish, given the interdependence of the two quantities (galaxies of higher masses tend to reside in higher density environments).

The latest observational data at both low and high redshifts has provoked a flurry of recent work aiming to understand the relationships between stellar mass, SFR and environment (e.g. Peng et al. 2010; Sobral et al. 2011; Scoville et al. 2013; Darvish et al. 2015). Both mass and environment are associated with transformations in colour, SFR and morphology, popularly known as 'quenching'. Supplementing low-redshift data from the SDSS (York & Adelman 2000) with higher redshift data from the zCOSMOS survey (Lilly et al. 2007), Peng et al. (2010) proposed that two primary quenching mechanisms, 'mass quenching' and 'environment quenching', act independently and dominate at different epochs and galaxy masses. 'Environment quenching', which primarily affects satellite galaxies (Peng et al. 2012), is attributed to some combination of gas stripping [due to ram pressure (Boselli & Gavazzi 2006) or tidal effects] and 'strangulation' (Larson 1980; Peng, Maiolino & Cochrane 2015), whereby gas is prevented from cooling on to the galaxy from its hot halo, perhaps upon accretion on to a massive halo. Mass quenching, which dominates the cessation of star formation for massive galaxies, is also attributed to a shut-down of cold gas accretion, via shock heating by the hot halo (Dekel & Birnboim 2006), possibly in combination with active galactic nucleus (AGN) heating (Best et al. 2006; Croton et al. 2006).

There is evidence that the trends observed at low redshift hold to at least $z \sim 1$. At $z \sim 1$, Sobral et al. (2011) and Muzzin et al. (2012) both find that the fraction of galaxies that are star forming decreases once we reach group densities and at high galaxy masses. However, things become less clear at even higher redshifts. Scoville et al. (2013) find a flattening in the relationship between environmental overdensity and both star-forming fraction and SFR above $z \sim 1.2$ for galaxies in the COSMOS field, and note that this flattening holds out to their highest redshift galaxies at $z \sim 3$. Other studies have found an apparent reversal of the low-z SFR (or morphology)–density relation at higher redshifts (Butcher & Oemler 1978). Both Sobral et al. (2011) and Elbaz et al. (2007) found that at $z \sim 1$, median galaxy SFR increases with overdensity until cluster densities are reached, at which point SFR decreases with overdensity, as in the local universe. Attempting to explain these opposing trends, McGee et al. (2009) propose that the pressure of the intracluster medium (ICM) on infalling galaxies in the outskirts of galaxy clusters actually compresses gas and enhances star formation prior to stripping in the denser environment of the cluster core. Increased galaxy–galaxy interactions may also trigger intense star formation via the disruption of gas discs. At high redshifts, high gas fractions (e.g. Tacconi et al. 2010) permit more efficient starburst responses. Thus at high redshifts, the richest environments may provide the combination of large gas reservoirs and ICM pressures that fuel high SFRs and later lead to quenching via gas exhaustion and stripping (Smail et al. 2014).

Quantifying the environmental dependence of star formation activity at high redshift directly is inherently challenging. An alternative approach to studying this is through autocorrelation functions of star-forming galaxies. The dark matter correlation function is the inverse Fourier transform of the dark matter power spectrum. Observing the projected real-space galaxy correlation function, which is a linear scaling of the dark matter correlation function, provides a natural connection between galaxies and the underlying matter distribution that determines their large-scale environments. Modelling these correlation functions using halo occupation distribution (HOD) model frameworks (Peacock & Smith 2000) can yield more information about galaxy host haloes, in particular their masses. It also provides a powerful technique for exploring the central/satellite dichotomy in galaxy populations. The 'one-halo' term represents clustering on small scales, within a single dark matter halo, and is determined by the spatial separation of central galaxies and their satellites. The 'two-halo' term, in contrast, is controlled by the larger-scale clustering of galaxies in different dark matter haloes (driven primarily by the halo mass), and incorporates central–central pairs as well as satellite–satellite and central–satellite correlations. A consistent picture has emerged in which more luminous and more massive star-forming galaxies tend to be more strongly clustered, as a result of lying preferentially in high-mass dark matter haloes. This holds both at low redshifts (e.g. Norberg et al. 2001; Zehavi et al. 2011) and at high redshifts (e.g. Sobral et al. 2010; Wake et al. 2011; Geach et al. 2012; Hatfield et al. 2016).

In this paper, we build upon the work presented in Sobral et al. (2010), which studied the clustering of ∼700 Hα emitters at $z = 0.84$ from the High-Redshift(Z) Emission Line Survey (HiZELS, see Section 2). Narrow-band (NB) Hα surveys such as HiZELS select only those galaxies with emission lines within a very narrow redshift range ($\Delta z \sim 0.02$) and with a well-defined redshift distribution. For clustering measurements, these types of survey are therefore superior to photometric ones, which are often hampered by systematic uncertainties and require a more complex treatment of the spatial distribution in the clustering analysis. Furthermore, unlike many spectroscopic surveys, the NB approach provides a clean selection function down to a known flux (SFR) limit. Sobral et al. (2010) found evidence for a strong Hα luminosity dependence of the clustering strength of Hα emitters at $z = 0.84$, along with evidence for a single relation with $L_{\mathrm{H}\alpha}/L^{*}_{\mathrm{H}\alpha}$ from $z \sim 0.2$ to ∼2.2. Geach et al. (2008, 2012) supplemented this work with the first analyses of the clustering of HiZELS galaxies at $z = 2.23$, though the sample was not sufficiently large to permit binning by luminosity.

Here, we analyse a larger sample of ∼3000 emitters at $z = 0.8$ spanning three fields: COSMOS, UDS and SA22. Crucially, we also use larger samples of Hα emitters at $z = 2.23$ and include new data at $z = 1.47$ (Sobral et al. 2012, 2013). Our samples, which span large ranges in Hα luminosity and redshift, provide optimal data for revealing the drivers of galaxy evolution over cosmic time. We provide details of the HiZELS sample selection in Section 2. In Section 3, we lay out our approach to quantifying the clustering of

Table 1. Numbers and mean redshifts of H α emitters identified by the HiZELS survey and selected for this analysis. HiZELS uses standard and custom-made NB filters, complemented by BB imaging, over well-studied fields. Only emitters that exceed the limiting flux, f_{50}, of their frames are included.

Field	$\bar{z}_{\mathrm{H}\alpha\ \mathrm{emitters}}$	No. emitters	Area (deg^2)
NBJ COSMOS & UDS	0.845 ± 0.011	503	1.6
LOW0H2 SA22	0.81 ± 0.011	2332	7.6
NBH COSMOS & UDS	1.47 ± 0.016	451	2.3
NBK COSMOS & UDS	2.23 ± 0.016	727	2.3

these sources via two-point correlation functions, and in Section 4, we present the results of simple power-law fits to these. Given the high quality of the correlation functions obtained, we extend these analyses to incorporate a sophisticated HOD modelling treatment. In Section 5, we set up the HOD framework and present derived halo properties for our HiZELS galaxies, in particular typical halo masses and galaxy central/satellite fractions. We discuss the implications of these results in Section 6.

We use a $H_0 = 70\,\mathrm{km\,s^{-1}\,Mpc^{-1}}$, $\Omega_\mathrm{M} = 0.3$ and $\Omega_\Lambda = 0.7$ cosmology throughout this paper.

2 THE HiZELS SURVEY AND SAMPLE SELECTION

2.1 Sample of H α emitters

HiZELS (Geach et al. 2008; Sobral et al. 2009, 2012, 2013) used the United Kingdom Infra-Red Telescope (UKIRT)'s Wide Field CAMera (WFCAM), the Subaru Telescope's Suprime-Cam with the NB921 filter, the Very Large Telescope (VLT)'s HAWK-I camera and the Canada–France–Hawaii Telescope (CFHT) with MegaCam (CFHiZELS; Sobral et al. 2015) to detect line emitters over large areas within well-studied fields. We present only a brief overview of the survey here, referring the curious reader to Sobral et al. (2013) for a full description of the HiZELS COSMOS and UDS data and to Sobral et al. (2015) for details of the SA22 CFHiZELS campaign.

HiZELS uses standard and custom-made NB filters, complemented by broad-band (BB) imaging. Sources identified by the NB filters are matched to those in the BB images by using the same aperture size and a search radius of 0.9 arcsec. True emitters are selected based on their NB–BB colour excess, with a signal-to-noise cut-off S/N > 3 and an equivalent width selection corresponding to EW > 25Å for H α. High-quality photometric redshifts derived from data spanning from optical to mid-IR wavelengths (e.g. Lawrence et al. 2007; Ilbert et al. 2009; Cirasuolo et al. 2010) were used to identify which emission line is being selected for each emitter, and thus select a clean sample of H α emitters. This technique enables the identical selection of H α emitting galaxies at $z = 0.81$, 0.84 (NBJ: COSMOS, UDS, SA22), $z = 1.47$ (NBH: COSMOS, UDS) and $z = 2.23$ (NBK: COSMOS, UDS); see Table 1 for details. Spectroscopic redshifts confirmed that the large sample of galaxies we obtain lies within well-defined redshift ranges (see also Sobral et al. 2016b; Stott et al. 2016).

H α fluxes are corrected for contamination by the adjacent [N II]$\lambda\lambda$6548, 6584 lines within the NB filter using the relationship between $\log([\mathrm{N\,II}]/\mathrm{H}\alpha)$ and $\mathrm{EW}_0([\mathrm{N\,II}] + \mathrm{H}\alpha)$ derived by Sobral et al. (2013) and confirmed spectroscopically in Sobral et al. (2015). They are also corrected for dust attenuation assuming $\mathrm{A}_{\mathrm{H}\alpha} = 1.0$ mag (Garn et al. 2010; Ibar et al. 2013). The median combined correction is 0.307 dex at $z = 0.8$, 0.325 dex at $z = 1.47$ and 0.335 dex at $z = 2.23$. Fig. 1 shows the corrected H α luminosity distributions at each redshift.

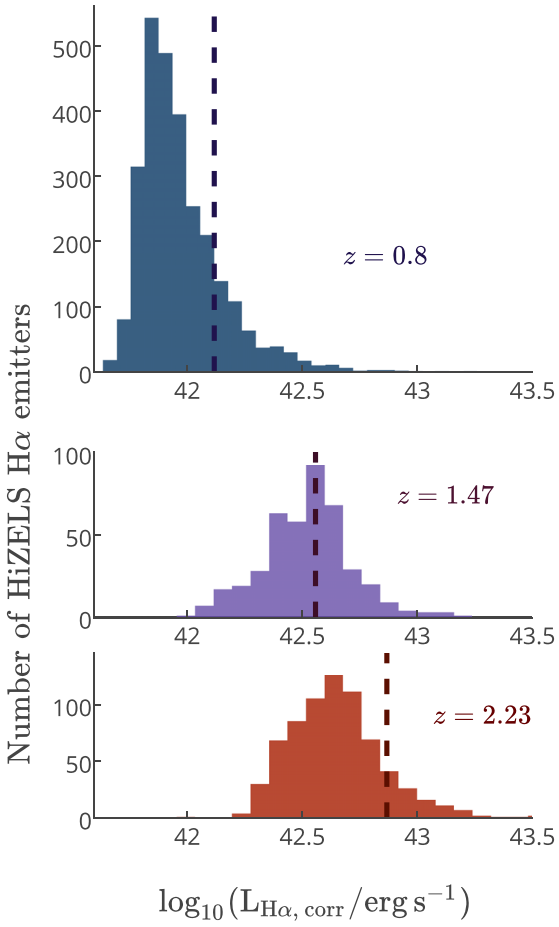

Figure 1. Distribution of dust-corrected H α luminosities of HiZELS emission line-selected galaxies in our samples at the three epochs. Vertical dashed lines show the characteristic luminosity, $L^*_{\mathrm{H}\alpha}$, at each redshift. HiZELS galaxies span a large luminosity range at each epoch, probing well below $L^*_{\mathrm{H}\alpha}$.

2.2 Generating random samples

We generated unclustered random samples in order to quantify the clustering of the observed H α emitters. Variations in coverage and observing conditions have resulted in individual HiZELS frames having different depths, meaning that robustly constructed random samples are essential to differentiate between true clustering and that introduced by the observing strategy. In this section, we describe the construction of random samples that reflect these depths.

Most simply, random sources may be generated by calculating a limiting flux at which each frame is essentially 100 per cent complete, drawing sources from the luminosity function (LF) down to this flux, and distributing these randomly across the frame. For this analysis, we aim to push further in flux, so as to include as many sources as possible. We include sources down to luminosities corresponding to the 50 per cent completeness flux, f_{50}, as calculated by Sobral et al. (2013, 2015) for each frame using Monte Carlo simulations. To study source detection as a function of the limiting flux (taking account of both incompleteness and flux boosting biases),

we have calculated the ratio of the number of sources recovered, $N_{\rm obs}$, to the number of sources expected from the LF, $N_{\rm LF}$, as a function of f_{50} in each frame. We found a small boost in the number of sources with recovered fluxes around the flux limit, suggesting that flux-boosting effects dominate over incompleteness. We tested different filters, and both deep and shallow fields separately, and found that all show the same general form. We have therefore fitted a single empirically derived effective completeness curve (the left-hand panel of Fig. 2) and taken this into account when generating the random catalogues. Numerous tests have confirmed that our results are qualitatively unchanged if the random sources are simply drawn from the LF down to f_{50} or constructed using a slightly different completeness curve.

In this paper, we use LF of the form:

$$\phi(L)\mathrm{d}L = \phi^* \left(\frac{L}{L^*}\right)^{\alpha} \mathrm{e}^{-(L/L^*)} \mathrm{d}\left(\frac{L}{L^*}\right), \quad (1)$$

where L^* represents the characteristic luminosity 'break' of the LF, ϕ^* is the corresponding characteristic comoving space density and α is the 'faint-end' slope of the power law, dominant at low luminosities. The parameters we adopt, given in Table 2, were derived using the samples of Hα emitters from Sobral et al. (2013, 2015). We generated a random position for each random source, carefully taking into account the boundaries of each frame and the masked regions due to bright stars and artefacts. The final number of sources generated within a frame depends on both its unmasked chip area and its depth. All random samples are substantially larger (e.g. 1000 $\times$) than the real samples. When constructing correlation functions for samples binned by flux, we also require knowledge of the fluxes of the random sources, to account for faint sources being preferentially detected in the deepest frames. The fluxes of random sources are drawn from the LF given in Table 2, scaled by the fitted completeness curve (Fig. 2) for a given f_{50}. We have also incorporated average corrections for dust and [N II] emission line contamination. We did not include any real or random sources with flux $f < f_{50}$ in this analysis.

Table 2. LF parameters used in this paper, derived in Sobral et al. (2013, 2015). At $z \sim 0.8$, we use the Schechter function fit to the much larger $z = 0.81$ sample by Sobral et al. (2015), which is more accurate than that presented by Sobral et al. (2013) and is also a good fit for the $z = 0.84$ data.

z	$L^*_{\mathrm{H}\alpha}$ (erg s^{-1})	ϕ^* (Mpc^{-3})	α
0.810 & 0.845	$42.12^{+0.03}_{-0.02}$	$-2.31^{+0.04}_{-0.05}$	$-1.6^{+0.2}_{-0.2}$
1.466	$42.56^{+0.06}_{-0.05}$	$-2.61^{+0.08}_{-0.09}$	$-1.62^{+0.25}_{-0.29}$
2.231	$42.87^{+0.08}_{-0.06}$	$-2.78^{+0.08}_{-0.09}$	$-1.59^{+0.12}_{-0.13}$

2.3 Effects of potential contaminants

Here, we discuss three classes of possible contaminants: sources that are not true emitters, true emitters that are different lines misclassified as Hα and AGN interlopers. As discussed in Section 2.1, HiZELS emitters are selected based on their NB–BB colour excess, with a signal-to-noise cut-off S/N $>$ 3. To check the possibility of including false emitters, we have repeated the clustering measurements using a more conservative cut-off S/N $>$ 4 for various luminosity bins. We find no significant differences in the clustering strengths. We also note that the exclusion of sources with fluxes below their frame's f_{50} serves to remove some potential low-flux contaminants. Contamination from misclassified lines is also estimated to be small, at $\sim$5 per cent, as estimated by Sobral et al. (2013). Such contaminants will generally have the effect of a small decrease in $w(\theta)$, with much smaller effects than our observed trends.

Our sample could suffer from contamination from AGN, for which Hα emission is not a reliable tracer of SFR. Using extensive multiwavelength data to identify AGN candidates within HiZELS samples in the COSMOS and UDS fields, Garn & Best (2010) estimate an AGN fraction of $\sim$10 per cent, but Sobral et al. (2016a) find that this can be much higher at very high Hα luminosities. We expect that the effect of AGN contamination may only be very important in the highest luminosity bins. However, these bins show no evidence of deviation from the linear trend of the low-luminosity regime (see Section 4.2). Given that it is difficult to exclude these individual sources from our analyses, we present all results using

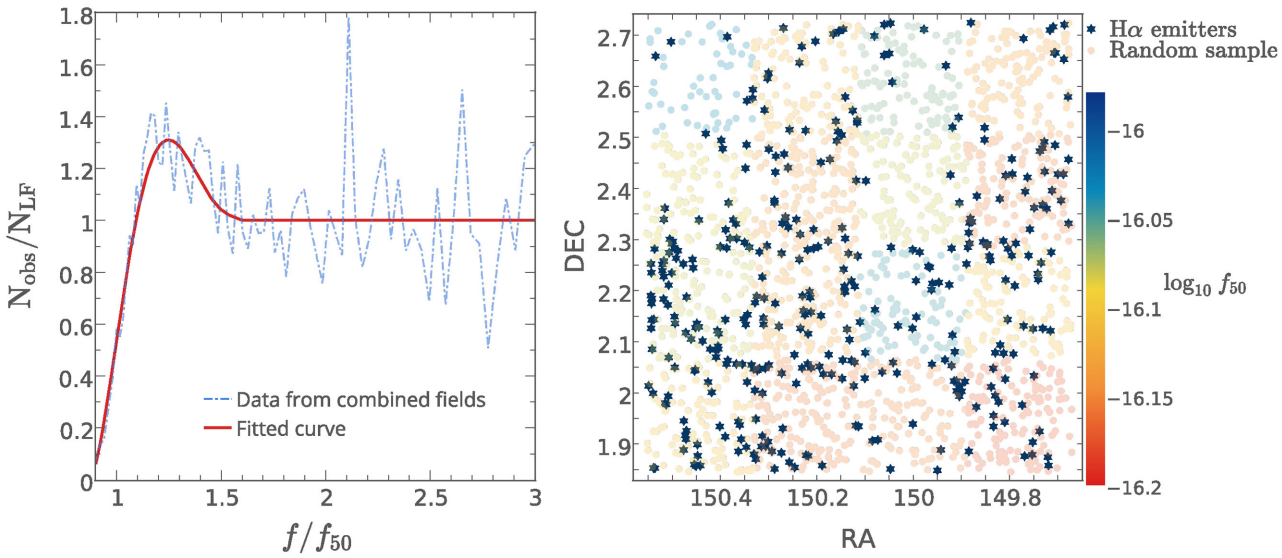

Figure 2. Left: the completeness curve used to place sources in frames with flux limit f_{50}. We account for a small number of excess sources due to flux boosting around the detection limit. Right: example of random sources in the COSMOS field, colour coded by the limiting flux of their frame, with real sources shown by stars overlaid. Fluxes are given in units of erg s^{-1}cm^{-2}.

Hα luminosity rather than converting to SFR explicitly. We invoke SFR only in our gas-regulator model interpretation in Section 6.2.

3 QUANTIFYING GALAXY CLUSTERING USING THE TWO-POINT CORRELATION FUNCTION

Broadly, the two-point correlation function compares the clustering of an observed sample to a uniformly distributed random sample with the same areal coverage. It quantifies overdensities on a large range of scales; unlike nearest-neighbour estimators, it can yield insights into both the local environment within haloes and the large-scale environment. When quantifying galaxy clustering, we construct correlation functions based on angular or projected distances between pairs of galaxies on the sky.

3.1 Angular two-point clustering statistics

The angular two-point correlation function, $w(\theta)$, is a popular estimator of the clustering strength of galaxies. It is defined as the excess probability of finding a pair of galaxies separated by a given angular distance, relative to that probability for a uniform (unclustered) distribution. The probability $\mathrm{d}P(\theta)$ of finding objects in solid angles $\mathrm{d}\Omega_1$ and $\mathrm{d}\Omega_2$ separated by angular distance θ is

$$\mathrm{d}P(\theta) = N^2(1 + w(\theta))\,\mathrm{d}\Omega_1\mathrm{d}\Omega_2, \tag{2}$$

where N is the surface density of objects.

Many estimators of $w(\theta)$ have been proposed. We use the minimum variance estimator proposed by Landy & Szalay (1993), which was shown to be less susceptible to bias from small sample sizes and fields:

$$w(\theta) = 1 + \left(\frac{N_\mathrm{R}}{N_\mathrm{D}}\right)^2 \frac{\mathrm{DD}(\theta)}{\mathrm{RR}(\theta)} - 2\frac{N_\mathrm{R}}{N_\mathrm{D}}\frac{\mathrm{DR}(\theta)}{\mathrm{RR}(\theta)}, \tag{3}$$

where N_R and N_D are the total number of random and data galaxies in the sample, and $\mathrm{RR}(\theta)$, $\mathrm{DD}(\theta)$ and $\mathrm{DR}(\theta)$ correspond to the number of random–random, data–data and data–random pairs separated by angle θ. $w(\theta)$ is normally fitted with a power law, $w(\theta) = A\theta^\beta$, where $\beta = -0.8$. Traditionally, Poissonian errors are used:

$$\Delta w(\theta) = \frac{1 + w(\theta)}{\sqrt{\mathrm{DD}(\theta)}}. \tag{4}$$

However, these errors are underestimates (e.g. see Norberg et al. 2009), since they do not account for cosmic variance or correlations between adjacent θ bins. Using these errors also gives unjustifiably large weightings to the largest angular separations, where large DD pair counts result in very low $\Delta w(\theta)$.

Norberg et al. (2009) conclude that whilst no internal estimator reproduces the error of external estimators faithfully, jackknife and bootstrap resampling methods perform reasonably well, although both overestimate the errors. They note that jackknife resampling estimates the large-scale variance accurately but struggles on smaller scales ($\sim$2–3 h^{-1} Mpc), with the resulting bias strongly dependent on the number of subvolumes. Bootstrap resampling, meanwhile, overestimates the variance by approximately 50 per cent on *all* scales, which may be minimized by oversampling the subvolumes. In this paper, we use the bootstrap resampling method with each correlation function constructed from 1000 bootstraps, taking the error on each $w(\theta)$ bin as the diagonal element of the bootstrap covariance matrix.

Table 3. Parameters of gaussian filter profile fits for the three HiZELS redshifts studied.

Redshift	$\mu(h^{-1}\,\mathrm{Mpc})$	$\sigma(h^{-1}\,\mathrm{Mpc})$
0.81 ± 0.011	1970	14
1.47 ± 0.016	3010	18
2.23 ± 0.016	3847	18

We also implement the integral constraint, IC (Groth & Peebles 1977), a small correction to account for the underestimation of clustering strength due to the finite area surveyed,

$$\mathrm{IC} = \frac{\sum_\theta \mathrm{A}\theta^\beta \mathrm{RR}(\theta)}{\sum_\theta \mathrm{RR}(\theta)}. \tag{5}$$

IC is small where fields are large. HiZELS fields reach square-degree scales, and so IC corrections are largely negligible.

3.2 Obtaining a real-space correlation length

In order to compare the clustering strengths of populations of star-forming galaxies at different redshifts quantitatively, we convert the angular correlation function to a spatial one. This conversion is often performed using Limber's approximation (Limber 1953), which assumes that spatial correlations that follow $\xi = (r/r_0)^\gamma$ are projected as angular correlation functions with slopes $\beta = \gamma + 1$. This results in the approximate relation between ξ and $w(\theta)$:

$$w(\theta) = \int_0^{+\infty} p_1(r)p_2(r)\mathrm{d}r \int_{-\infty}^{+\infty} r\xi(R, r)\mathrm{d}\Delta, \tag{6}$$

where $R = \sqrt{r^2\theta^2 + \Delta r^2}$, and $p_1(r)$, $p_2(r)$ are the filter profiles for projected fields 1 and 2. Substituting $\xi = (r/r_0)^\gamma$ yields

$$w(\theta) = r_0^\gamma \theta(\mathrm{rad})^{1-\gamma} \times \frac{\Gamma(\gamma/2 - 1/2)\Gamma(1/2)}{\Gamma(\gamma/2)} \times \int_0^{+\infty} p_1(r)p_2(r)r^{1-\gamma}\mathrm{d}r, \tag{7}$$

where $\Gamma(x)$ is the gamma function. This is a good approximation for small angular scales, where $\theta \ll \sigma/\mu$, and can thus be used to evaluate r_0 from the fitted $w(\theta)$ profile. However, the integral diverges for narrow filters. Simon (2007) shows that in the limiting case of a delta function filter, the observed $w(\theta)$ is no longer a projection, but simply a rescaled $\xi_\mathrm{gal}(r)_0$ (thus $\beta = \gamma$ at large separations). Since Limber's approximation is not reliable for our samples of galaxies, which span fields with separations of degrees and use very narrow filters, we perform a numerical integration of the exact equation:

$$w_\mathrm{model}(\theta) = \psi^{-1} \int_0^{+\infty} \int_{s\sqrt{2\phi}}^{2s} \frac{2f_s(s - \Delta)f_s(s + \Delta)}{R^{-\gamma-1}r_0^\gamma \Delta}\mathrm{d}R\mathrm{d}s, \tag{8}$$

where, $\psi = 1 + \cos\theta$, $\phi = 1 - \cos\theta$, $\Delta = \sqrt{(R^2 - 2s^2\phi)/2\psi}$ and f_s is the profile of the filter, fitted as a Gaussian profile with μ and σ that depend on the filter being considered (see Table 3 for the parameters of our filters). We assume that the standard value of $\gamma = -1.8$. χ^2 fitting of observed against modelled $w(\theta)$, generated using different r_0, allows us to estimate r_0 and its error (following Sobral et al. 2010).

3.2.1 *Projected-space two-point clustering statistics*

The clustering statistic required as input for the halo fitting routine we use in Section 5.3 is the projected-space (r_p) two-point

correlation function, $w_p(r_p)$. We therefore transform our measured $w(\theta)$ to $w_p(r_p)$. $w_p(r_p)$ is defined by first considering the spatial two-point correlation function along the line of sight (r_l) and perpendicular to the line of sight (r_p):

$$\xi(r_p, r_l) = 1 + \left(\frac{N_\mathrm{R}}{N_\mathrm{D}}\right)^2 \frac{\mathrm{DD}(r_p, r_l)}{\mathrm{RR}(r_p, r_l)} - 2\frac{N_\mathrm{R}}{N_\mathrm{D}} \frac{\mathrm{DR}(r_p, r_l)}{\mathrm{RR}(r_p, r_l)}. \quad (9)$$

$\xi(r_p, r_l)$ is then integrated over r_l to obtain $w_p(r_p)$:

$$w_p(r_p) = 2\int_0^{r_{l,\max}} \xi(r_p, r_l)\mathrm{d}r_l. \quad (10)$$

This is related to the real-space correlation function by

$$w_p(r_p) = 2\int_{r_p}^{+\infty} \frac{r\xi(r)}{(r^2 - r_p^2)^{1/2}}\mathrm{d}r \quad (11)$$

in the limit of a wide filter, and the solution tends to

$$w_p(r_p) = r_p \left(\frac{r_p}{r_0}\right)^{-\gamma} \frac{\Gamma(\gamma/2 - 1/2)\Gamma(1/2)}{\Gamma(\gamma/2)}. \quad (12)$$

In the case of a narrower top-hat filter, we integrate over a finite range of r_l, using $(r_p^2 + r_{l,\max}^2)^{1/2}$ as the upper limit to the integral in equation (11).

In this paper, we calculate $w_p(r_p)$ from our observed $w(\theta)$. However, our filter profiles are not top-hat (as assumed for the integral in equation 11) but are better approximated by Gaussian profiles (see Table 3 for parameters). To account for this difference, we perform numerical integrations to determine the factor by which $w(\theta)$ differs [for a given $\xi(r)$] if observed over a top-hat of width 2σ as opposed to a Gaussian of width σ (changing f_s in equation 8); we find a required correction of $\sqrt{\pi}$. Using this, and combining equations (3), (9) and (10), with $r_p = \mathrm{D_{ang}}\theta(\mathrm{rad})$, we then obtain

$$w_p(r_p) \sim 2\sigma\sqrt{\pi}\, w\left(\theta = \frac{r_p}{\mathrm{D_{ang}}}\right)(1+z)^{0.8}. \quad (13)$$

4 RESULTS FROM POWER-LAW FITS TO THE ANGULAR CORRELATION FUNCTION

4.1 Whole samples at well-defined redshifts

We have derived angular correlation functions for large samples of Hα emitters at each redshift and fitted these with power-law models (see Fig. 3). The exact luminosity ranges of these samples, given in Table 4, are chosen to compare similar samples at each redshift, and span the same range in $L_{\mathrm{H}\alpha}/L^*_{\mathrm{H}\alpha}$: $-0.4 < \log_{10}(L_{\mathrm{H}\alpha}/L^*_{\mathrm{H}\alpha}) < 0.3$ (albeit with non-matched distributions within this range). The fits shown are those described in Section 3.2, with a power law of fixed gradient -1.8 for the spatial correlation function, leading to a slope of -0.8 in the angular correlation function on small scales and the correction to Limber's approximation at large scales where the angular separation is much greater than the separation along the line of sight. This parametrization is sufficient to derive indicative clustering strengths. However, the correlation functions of all three samples do show clear departures from the traditional power-law relation fitted here. At angular scales of the order of 10s of arcseconds, the power-law fit consistently overestimates the observed $w(\theta)$, indicative of a dominant contribution from a separate one-halo term at small angular separations. We explore this further in Section 5.

4.2 Clustering strength as a function of galaxy H α luminosity

We have fitted both luminosity-binned data and luminosity-limited data with the same power-law models (see Table 4 and Appendix A). As shown in the lower panels of Fig. 3, the clustering strength, r_0, increases roughly linearly with galaxy Hα luminosity for the luminosity-binned samples, showing that more highly star-forming galaxies are more strongly clustered, and hence may live in more massive dark matter halo environments. The trends are similar for the luminosity-limited samples: these also show an increase in clustering strength with galaxy luminosity. The results for the two sample types do not agree exactly because luminosity-limited samples of galaxies with faint limits have their clustering increased by the inclusion of a small number of bright sources, and therefore have a greater clustering strength than that of galaxies entirely within a faint luminosity bin.

Although the absolute values of r_0 agree (within errors) with the previous HiZELS study of a smaller sample of Hα emitters at $z = 0.8$, the apparently linear relationship is at odds with the results of Sobral et al. (2010), who found tentative hints of a more step-like behaviour around the characteristic luminosity. With our much larger sample of ~3000 emitters, there is no longer evidence for a break in the r_0 versus $\log_{10}(L_{\mathrm{H}\alpha})$ relationship, and a linear relation provides a far better fit. The trends at $z = 1.47$ and 2.23 also show no clear departure from a simple linear trend, albeit that the $z \sim 1.47$ results are noisier. These results are also broadly consistent with previous studies. We find $r_0 = 4.3^{+0.5}_{-0.4}\,h^{-1}$ Mpc for our sample at $z = 1.47$, whilst Kashino et al. (2017) obtain $r_0 = 5.2 \pm 0.7\,h^{-1}$ Mpc for Hα emitters at $1.43 \leq z \leq 1.74$. We find $r_0 = 4.7^{+0.5}_{-0.4}\,h^{-1}$ Mpc for the full sample at $z = 2.23$, which is slightly higher than Geach et al. (2012) found using a smaller sample at the same redshift ($r_0 = 3.7 \pm 0.3$), but this depends critically on the luminosity range studied.

In Fig. 4, we show the Hα luminosity-dependent clustering of $z = 0.8$ HiZELS emitters split into two observed K-band magnitude bins. Observed K-band magnitude is believed to be a rough proxy for galaxy stellar mass. We find that the clustering strength increases broadly linearly with $\log_{10}(L_{\mathrm{H}\alpha})$ within each of the broad K-band magnitude bins and that this trend is much larger than any differences between the two K-band magnitude bins. We will explore the stellar mass-dependence of the clustering of star-forming galaxies more thoroughly in a subsequent paper, but we stress here that the strong trends of clustering strength with Hα luminosity presented in this paper are not driven primarily by galaxy stellar mass.

5 MODELLING GALAXY POPULATIONS VIA HOD FITTING

The HOD formalism extends dark matter halo models to galaxy populations: given a set of input parameters, we can predict the average number of galaxies of a certain type as a function of dark matter halo mass, $\langle N|M\rangle$. A combination of a cosmological model and an HOD enables us to predict any clustering statistic on any scale; usually observations of galaxy clustering (or weak lensing) are then used to constrain cosmological or galaxy evolution models. Here, HOD modelling enables us to estimate typical host halo masses for HiZELS galaxies. We can also do better than the straight-line r_0 fit; HOD fitting takes into account the small dip observed on angular scales of the order of 10 s of arcseconds, below which the clustering is dominated by correlations between galaxies within a single dark

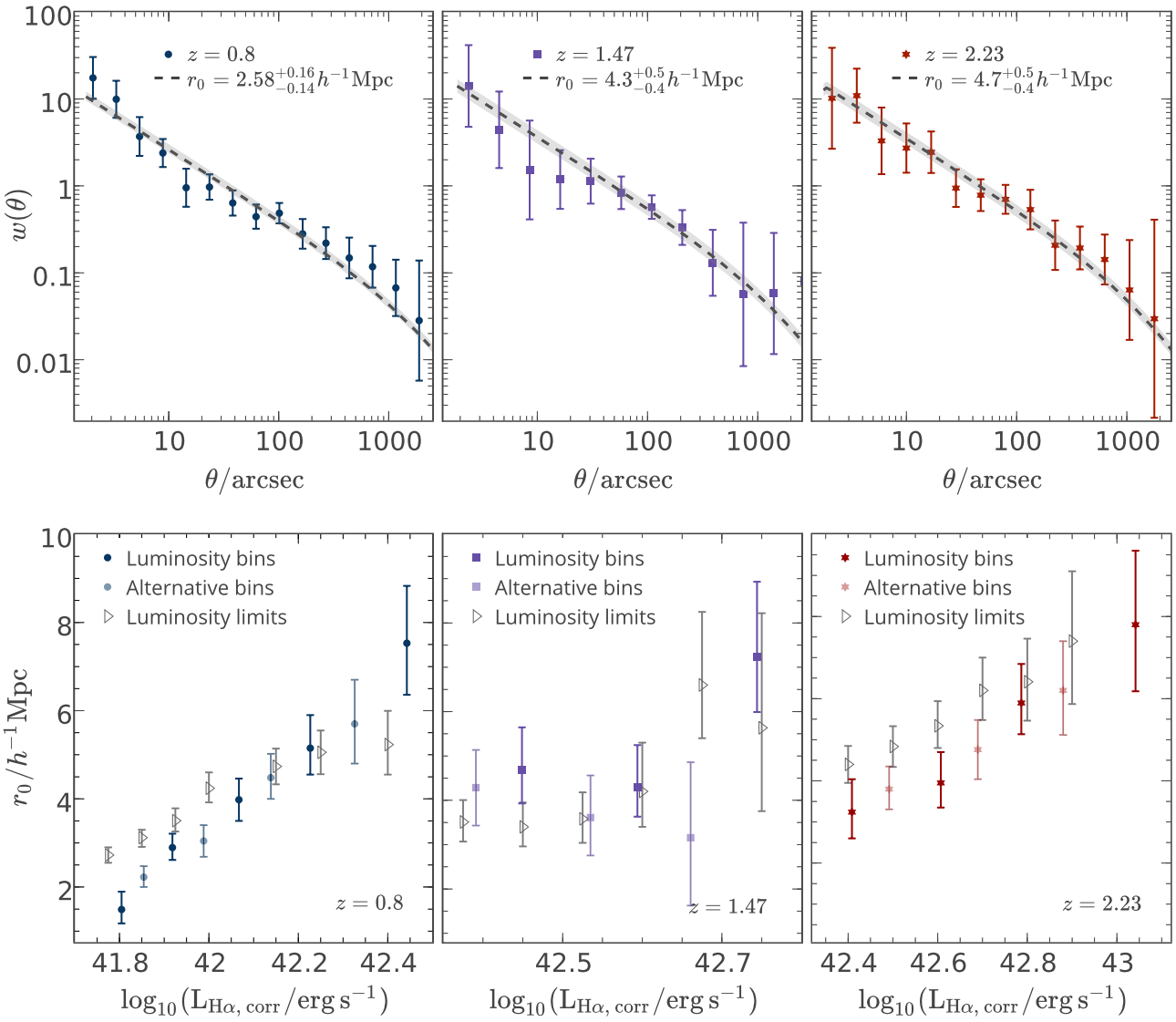

Figure 3. Top: power-law fits (with the correction to Limber's approximation at large scales) to the measured angular correlation functions at three redshifts, each over the same range in $L_{H\alpha}/L^*_{H\alpha}$. Bottom: derived clustering strength, r_0, for Hα luminosity-binned and luminosity-limited samples. We also show alternative binning. The plotted luminosity value is the mean value of $\log_{10}(L_{H\alpha})$ for the luminosity-binned samples, and the lower limit for the luminosity-limited samples. The clustering strength increases with $\log_{10}L_{H\alpha}$ for all three redshifts surveyed in a broadly linear manner.

matter halo. We can now include the effects of the satellite galaxy population on the observed clustering, no longer assuming that a power-law relationship holds on the smallest scales.

A number of different halo occupation parametrizations have been used to fit two-point galaxy correlation functions. Typically, three or five-parameter fits of Zehavi et al. (2005) and Zheng et al. (2005) are used. Whilst these do well for stellar mass-selected samples (e.g. Wake et al. 2011; Hatfield et al. 2016), they may not be suitable for our sample. As noted by Contreras et al. (2013), HODs for stellar mass-selected samples are very different to the HODs of SFR or cold gas mass-selected samples. In particular, HODs for mass-selected samples sensibly assume that above a given halo mass, all haloes contain a central galaxy. However, in not all cases does this central galaxy fall within an SFR or cold gas selected sample (e.g. due to the suppression of gas cooling in high-mass haloes via AGN feedback), so for SFR-limited samples the HOD for central galaxies may be peaked rather than a step function (Contreras et al. 2013).

5.1 An eight-parameter HOD model

Studying the clustering hsides of Hα emitters at $z = 2.23$, Geach et al. (2012) developed an eight-parameter model suitable for star formation selected samples via comparison to the predictions of the semi-analytic model GALFORM (Cole et al. 2000; Bower et al. 2006). In this parametrization, the mean numbers of central[1] and satellite galaxies in a halo of mass M are given by

$$\langle N_{\rm cen}|M\rangle = F_c^B(1-F_c^A)\exp\left[-\frac{\log(M/M_{\rm c})^2}{2(\sigma_{\log M})^2}\right] + \frac{1}{2}F_c^A\left[1+\mathrm{erf}\left(\frac{\log(M/M_{\rm c})}{\sigma_{\log M}}\right)\right], \quad (14)$$

[1] In Geach et al. (2012), the factor of $\frac{1}{2}$ in the second term of the central galaxy parametrization was excluded. We include it here, so that a halo can host a maximum of one (rather than two) central galaxies.

Table 4. r_0 values and key parameters derived from HOD fitting, for samples of Hα emitters at different redshifts and luminosities. We find a clear trend towards increasing r_0, $b_{\rm eff}$, $M_{\rm min}$ and $M_{\rm eff}$ for samples of galaxies with higher Hα luminosities at all redshifts, but little evidence for changing satellite fractions for these SFR-selected samples.

Redshift	$\log_{10}(L_{\rm H\alpha}$ range/erg s^{-1})	Mean $\log_{10}(L_{\rm H\alpha})$	r_0/h^{-1} Mpc	$b_{\rm eff}$	$\log_{10}(M_{\rm eff}/{\rm M}_\odot)$	$\log_{10}(M_{\rm min}/{\rm M}_\odot)$	$f_{\rm sat}$
'Full' samples: $-0.4 < \log_{10}(L_{\rm H\alpha}/L^*_{\rm H\alpha}) < 0.3$							
0.8	41.72–42.42	41.96	$2.6^{+0.2}_{-0.1}$	$1.12^{+0.06}_{-0.05}$	$12.13^{+0.10}_{-0.09}$	$11.12^{+0.11}_{-0.15}$	$0.05^{+0.01}_{-0.01}$
1.47	42.16–42.86	42.52	$4.3^{+0.5}_{-0.4}$	$1.78^{+0.06}_{-0.08}$	$12.16^{+0.07}_{-0.09}$	$11.45^{+0.06}_{-0.08}$	$0.05^{+0.02}_{-0.02}$
2.23	42.47–43.17	42.71	$4.7^{+0.5}_{-0.4}$	$2.52^{+0.07}_{-0.09}$	$11.96^{+0.05}_{-0.07}$	$11.41^{+0.06}_{-0.06}$	$0.05^{+0.02}_{-0.02}$
Hα luminosity-selected subsamples							
	Bins						
0.8	41.7–41.85	41.80	$1.5^{+0.4}_{-0.3}$	$1.07^{+0.09}_{-0.03}$	$11.92^{+0.14}_{-0.04}$	$11.26^{+0.13}_{-0.08}$	$0.03^{+0.01}_{-0.01}$
0.8	41.775–41.925	41.85	$2.2^{+0.3}_{-0.2}$	$1.16^{+0.06}_{-0.03}$	$12.01^{+0.14}_{-0.06}$	$11.46^{+0.08}_{-0.07}$	$0.02^{+0.01}_{-0.01}$
0.8	41.85–42.0	41.92	$2.9^{+0.3}_{-0.3}$	$1.33^{+0.07}_{-0.06}$	$12.31^{+0.14}_{-0.11}$	$11.69^{+0.07}_{-0.08}$	$0.02^{+0.01}_{-0.01}$
0.8	41.925–42.075	41.99	$3.1^{+0.4}_{-0.4}$	$1.32^{+0.09}_{-0.07}$	$12.30^{+0.16}_{-0.12}$	$11.71^{+0.10}_{-0.10}$	$0.02^{+0.01}_{-0.01}$
0.8	42.0–42.15	42.07	$4.0^{+0.5}_{-0.5}$	$1.49^{+0.08}_{-0.09}$	$12.55^{+0.11}_{-0.14}$	$11.91^{+0.08}_{-0.12}$	$0.02^{+0.01}_{-0.01}$
0.8	42.075–42.25	42.14	$4.5^{+0.5}_{-0.5}$	$1.56^{+0.07}_{-0.09}$	$12.63^{+0.08}_{-0.12}$	$12.01^{+0.07}_{-0.09}$	$0.02^{+0.01}_{-0.01}$
0.8	42.15–42.35	42.23	$5.2^{+0.8}_{-0.6}$	$1.63^{+0.08}_{-0.11}$	$12.71^{+0.09}_{-0.13}$	$12.09^{+0.07}_{-0.12}$	$0.03^{+0.02}_{-0.01}$
0.8	42.25–42.475	42.33	$5.7^{+1.0}_{-0.9}$	$1.79^{+0.08}_{-0.12}$	$12.86^{+0.07}_{-0.12}$	$12.28^{+0.07}_{-0.11}$	$0.03^{+0.02}_{-0.01}$
0.8	42.35–42.6	42.44	$7.5^{+1.3}_{-1.2}$	$2.02^{+0.08}_{-0.13}$	$13.05^{+0.06}_{-0.10}$	$12.50^{+0.06}_{-0.09}$	$0.05^{+0.03}_{-0.02}$
	Limits						
0.8	>41.775	41.99	$2.7^{+0.2}_{-0.2}$	$1.18^{+0.06}_{-0.06}$	$12.18^{+0.10}_{-0.11}$	$11.24^{+0.10}_{-0.14}$	$0.04^{+0.01}_{-0.01}$
0.8	>41.85	42.03	$3.1^{+0.2}_{-0.2}$	$1.26^{+0.05}_{-0.06}$	$12.28^{+0.08}_{-0.11}$	$11.40^{+0.08}_{-0.11}$	$0.04^{+0.01}_{-0.01}$
0.8	>41.925	42.10	$3.5^{+0.3}_{-0.3}$	$1.32^{+0.05}_{-0.07}$	$12.38^{+0.08}_{-0.11}$	$11.54^{+0.07}_{-0.10}$	$0.04^{+0.01}_{-0.01}$
0.8	>42.0	42.18	$4.2^{+0.4}_{-0.3}$	$1.41^{+0.05}_{-0.07}$	$12.52^{+0.07}_{-0.10}$	$11.69^{+0.07}_{-0.09}$	$0.05^{+0.02}_{-0.02}$
0.8	>42.075	42.25	$4.7^{+0.4}_{-0.4}$	$1.48^{+0.05}_{-0.07}$	$12.57^{+0.06}_{-0.09}$	$11.84^{+0.07}_{-0.09}$	$0.03^{+0.02}_{-0.01}$
0.8	>42.15	42.33	$5.1^{+0.5}_{-0.5}$	$1.57^{+0.06}_{-0.08}$	$12.66^{+0.07}_{-0.10}$	$11.98^{+0.07}_{-0.09}$	$0.03^{+0.02}_{-0.01}$
0.8	>42.25	42.44	$5.2^{+0.8}_{-0.7}$	$1.71^{+0.07}_{-0.11}$	$12.79^{+0.07}_{-0.12}$	$12.18^{+0.07}_{-0.10}$	$0.03^{+0.02}_{-0.01}$
0.8	>42.4	42.57	$5.8^{+1.5}_{-1.3}$	$2.00^{+0.11}_{-0.17}$	$13.03^{+0.09}_{-0.14}$	$12.53^{+0.07}_{-0.13}$	$0.03^{+0.02}_{-0.01}$
	Bins						
1.47	42.3–42.45	42.39	$4.3^{+0.9}_{-0.8}$	$2.12^{+0.09}_{-0.13}$	$12.4^{+0.07}_{-0.12}$	$11.88^{+0.06}_{-0.10}$	$0.02^{+0.01}_{-0.01}$
1.47	42.375–42.525	42.45	$4.7^{+1.0}_{-0.9}$	$2.21^{+0.09}_{-0.13}$	$12.48^{+0.06}_{-0.11}$	$11.97^{+0.06}_{-0.09}$	$0.02^{+0.01}_{-0.01}$
1.47	42.45–42.6	42.53	$3.6^{+1.0}_{-0.7}$	$2.12^{+0.16}_{-0.15}$	$12.39^{+0.14}_{-0.14}$	$11.97^{+0.09}_{-0.11}$	$0.01^{+0.01}_{-0.01}$
1.47	42.525–42.675	42.59	$4.3^{+1.0}_{-0.9}$	$2.21^{+0.20}_{-0.18}$	$12.46^{+0.15}_{-0.15}$	$12.04^{+0.10}_{-0.16}$	$0.03^{+0.01}_{-0.01}$
1.47	42.6–42.75	42.66	$3.2^{+1.7}_{-1.2}$	$2.28^{+0.22}_{-0.18}$	$12.50^{+0.16}_{-0.15}$	$12.12^{+0.11}_{-0.13}$	$0.02^{+0.01}_{-0.01}$
1.47	42.675–42.85	42.74	$7.2^{+1.7}_{-1.5}$	$2.72^{+0.13}_{-0.20}$	$12.79^{+0.07}_{-0.11}$	$12.34^{+0.07}_{-0.12}$	$0.07^{+0.06}_{-0.04}$
1.47	42.75–43.3	42.87	$6.8^{+2.6}_{-2.2}$	$2.67^{+0.16}_{-0.26}$	$12.76^{+0.09}_{-0.16}$	$12.33^{+0.07}_{-0.15}$	$0.04^{+0.03}_{-0.02}$
	Limits						
1.47	>42.2	42.55	$3.7^{+0.5}_{-0.4}$	$1.85^{+0.07}_{-0.11}$	$12.18^{+0.08}_{-0.12}$	$11.58^{+0.06}_{-0.10}$	$0.02^{+0.01}_{-0.01}$
1.47	>42.375	42.59	$3.5^{+0.5}_{-0.4}$	$1.90^{+0.09}_{-0.12}$	$12.22^{+0.09}_{-0.13}$	$11.67^{+0.07}_{-0.10}$	$0.02^{+0.01}_{-0.01}$
1.47	>42.45	42.63	$3.4^{+0.6}_{-0.4}$	$1.90^{+0.16}_{-0.13}$	$12.21^{+0.16}_{-0.15}$	$11.71^{+0.09}_{-0.13}$	$0.02^{+0.01}_{-0.01}$
1.47	>42.525	42.66	$3.6^{+0.6}_{-0.5}$	$2.07^{+0.12}_{-0.14}$	$12.36^{+0.11}_{-0.13}$	$11.88^{+0.08}_{-0.10}$	$0.02^{+0.01}_{-0.01}$
1.47	>42.6	42.73	$4.2^{+1.1}_{-0.8}$	$2.22^{+0.14}_{-0.17}$	$12.47^{+0.11}_{-0.14}$	$12.02^{+0.08}_{-0.12}$	$0.02^{+0.01}_{-0.01}$
1.47	>42.675	42.80	$6.6^{+1.7}_{-1.2}$	$2.56^{+0.12}_{-0.18}$	$12.71^{+0.07}_{-0.11}$	$12.22^{+0.07}_{-0.11}$	$0.07^{+0.06}_{-0.04}$
1.47	>42.75	42.87	$5.6^{+2.6}_{-1.9}$	$2.69^{+0.14}_{-0.25}$	$12.77^{+0.08}_{-0.15}$	$12.34^{+0.07}_{-0.14}$	$0.03^{+0.03}_{-0.02}$
	Bins						
2.23	42.2–42.5	42.41	$3.2^{+0.8}_{-0.6}$	$2.30^{+0.11}_{-0.17}$	$11.79^{+0.09}_{-0.15}$	$11.25^{+0.07}_{-0.13}$	$0.03^{+0.02}_{-0.01}$
2.23	42.35–42.6	42.49	$3.8^{+0.6}_{-0.5}$	$2.50^{+0.10}_{-0.15}$	$11.93^{+0.07}_{-0.12}$	$11.43^{+0.06}_{-0.09}$	$0.02^{+0.01}_{-0.01}$
2.23	42.5–42.7	42.61	$4.0^{+0.8}_{-0.6}$	$2.67^{+0.13}_{-0.20}$	$12.03^{+0.09}_{-0.14}$	$11.58^{+0.07}_{-0.12}$	$0.02^{+0.01}_{-0.01}$
2.23	42.6–42.8	42.69	$4.8^{+0.7}_{-0.7}$	$2.87^{+0.09}_{-0.16}$	$12.14^{+0.06}_{-0.10}$	$11.70^{+0.05}_{-0.09}$	$0.02^{+0.01}_{-0.01}$
2.23	42.7–42.9	42.79	$5.9^{+1.0}_{-0.8}$	$3.05^{+0.09}_{-0.14}$	$12.24^{+0.05}_{-0.08}$	$11.81^{+0.05}_{-0.07}$	$0.02^{+0.01}_{-0.01}$
2.23	42.8–43.0	42.88	$6.2^{+1.2}_{-1.1}$	$3.23^{+0.10}_{-0.16}$	$12.33^{+0.05}_{-0.08}$	$11.92^{+0.05}_{-0.07}$	$0.03^{+0.02}_{-0.01}$
2.23	42.9–43.6	43.04	$7.8^{+1.8}_{-1.6}$	$3.23^{+0.11}_{-0.19}$	$12.35^{+0.05}_{-0.09}$	$11.93^{+0.05}_{-0.08}$	$0.05^{+0.03}_{-0.03}$

Table 4 – *continued*

Redshift	$\log_{10}(L_{\mathrm{H}\alpha}$ range/erg s^{-1})	Mean $\log_{10}(L_{\mathrm{H}\alpha})$	r_0/h^{-1} Mpc	b_{eff}	$\log_{10}(M_{\mathrm{eff}}/\mathrm{M}_\odot)$	$\log_{10}(M_{\mathrm{min}}/\mathrm{M}_\odot)$	f_{sat}
	Limits						
2.23	>42.2	42.66	$4.3^{+0.5}_{-0.4}$	$2.23^{+0.07}_{-0.09}$	$11.77^{+0.06}_{-0.08}$	$11.12^{+0.06}_{-0.07}$	$0.07^{+0.02}_{-0.02}$
2.23	>42.3	42.66	$4.3^{+0.5}_{-0.4}$	$2.29^{+0.07}_{-0.09}$	$11.80^{+0.05}_{-0.08}$	$11.21^{+0.06}_{-0.07}$	$0.04^{+0.02}_{-0.01}$
2.23	>42.4	42.69	$4.4^{+0.5}_{-0.5}$	$2.39^{+0.07}_{-0.11}$	$11.86^{+0.06}_{-0.10}$	$11.30^{+0.06}_{-0.07}$	$0.04^{+0.01}_{-0.01}$
2.23	>42.5	42.73	$4.8^{+0.5}_{-0.5}$	$2.52^{+0.07}_{-0.10}$	$11.95^{+0.05}_{-0.08}$	$11.42^{+0.05}_{-0.07}$	$0.04^{+0.02}_{-0.01}$
2.23	>42.6	42.78	$5.3^{+0.6}_{-0.5}$	$2.65^{+0.08}_{-0.12}$	$12.03^{+0.05}_{-0.09}$	$11.53^{+0.05}_{-0.07}$	$0.04^{+0.01}_{-0.01}$
2.23	>42.7	42.87	$6.2^{+0.8}_{-0.7}$	$2.83^{+0.08}_{-0.12}$	$12.14^{+0.05}_{-0.07}$	$11.66^{+0.05}_{-0.07}$	$0.04^{+0.02}_{-0.02}$
2.23	>42.8	42.95	$6.4^{+1.1}_{-1.0}$	$3.03^{+0.09}_{-0.15}$	$12.24^{+0.05}_{-0.09}$	$11.79^{+0.05}_{-0.07}$	$0.04^{+0.02}_{-0.02}$
2.23	>42.9	43.06	$7.4^{+1.7}_{-1.5}$	$3.26^{+0.12}_{-0.19}$	$12.35^{+0.06}_{-0.10}$	$11.93^{+0.05}_{-0.08}$	$0.05^{+0.04}_{-0.03}$

$$\langle N_{\mathrm{sat}}|M\rangle = F_s\left[1+\mathrm{erf}\left(\frac{\log(M/M_{\mathrm{min}})}{\delta_{\log M}}\right)\right]\left(\frac{M}{M_{\mathrm{min}}}\right)^{\alpha}. \quad (15)$$

The key parameters are as follows:

(i) M_{c}: the halo mass at which the probability of hosting a central galaxy peaks.

(ii) $\sigma_{\log M}$: the width of the Gaussian distribution of centrals around its peak, M_{c}.

(iii) M_{min}: the threshold halo mass for satellite galaxies, above which the distribution follows a power law $\langle N_{\mathrm{sat}}|M\rangle \approx F_s(\frac{M}{M_{\mathrm{min}}})^{\alpha}$.

(iv) $\delta_{\log M}$: characterizes the width of the transition to $\langle N_{\mathrm{sat}}|M\rangle = F_s(\frac{M}{M_{\mathrm{min}}})^{\alpha}$ around M_{min}.

(v) α: the slope of the power law for $\langle N_{\mathrm{sat}}|M\rangle$ in haloes with $M > M_{\mathrm{min}}$.

(vi) $F_c^{A,B}$: normalization factors in range [0,1].

(vii) F_s: the mean number of satellite galaxies per halo at $M = M_{\mathrm{min}}$.

Geach et al. (2012) did not have large enough samples to fit all eight parameters simultaneously, so fixed the following parameters:

(i) $M_{\mathrm{c}} = M_{\mathrm{min}}$. The minimum mass halo hosting a satellite galaxy is the mass at which the central HOD peaks.

(ii) $\sigma_{\log M} = \delta_{\log M}$. The smoothing of the low-mass cut-off for satellite galaxies is not critical, as satellites in low-mass haloes contribute little to the overall HOD.

(iii) $\alpha = 1$. This is consistent with the literature for mass-selected samples.

The total number of galaxies is given by

$$\langle N|M\rangle = \langle N_{\mathrm{cen}}|M\rangle + \langle N_{\mathrm{sat}}|M\rangle. \quad (16)$$

Some implementations use $\langle N|M\rangle = \langle N_{\mathrm{cen}}|M\rangle[1 + \langle N_{\mathrm{sat}}|M\rangle]$, requiring a central for every satellite galaxy. Given that our sample is essentially SFR-limited, some of our galaxies could be star-forming satellites around less highly star-forming centrals that are not included in our sample. Therefore, we do not impose this condition.

We have performed a number of tests with different HOD parametrizations (e.g. allowing α to vary, fitting a full eight-parameter model) and confirm that neither the reproduction of the correlation function nor the values of the derived parameters are dependent on our choice (see Appendix B1). We base our parametrization on the five-parameter model of Geach et al. (2012), but truncate the halo occupation sharply at M_{min}, allowing only haloes more massive than this to host galaxies. As detailed in Appendix B2, we have found that allowing the HOD to reach lower halo masses results in values of M_{min} that are strongly dependent on the lower limit of the HOD integral, and which are poorly constrained. M_{min} is now the minimum mass of halo hosting central galaxies and, due to the shape of the halo mass function, also the most common host halo mass. Reassuringly, all other derived parameters are robust against the choice of lower limit.

5.2 Physical parameters from HOD models

When fitting the models to data, we use the observed number density of galaxies as a constraint. For a given $\langle N|M\rangle$ output from the halo model, the predicted number density of galaxies is

$$n_{\mathrm{g}} = \int \mathrm{d}M n(M)\langle N|M\rangle, \quad (17)$$

where $n(M)$ is the halo mass function. Here, we use that of Tinker et al. (2010). The observed number density of galaxies used is the integral of the LF between the same limits used to select the real and random galaxy sample (using the LF derived by Sobral et al. 2013, 2015 for the same data). We assume a 10 per cent error on the number density in the fitting.

For each set of HOD parameters, we may derive a number of parameters of interest for galaxy evolution. The satellite fraction is

$$f_{\mathrm{sat}} = \frac{1}{n_{\mathrm{g}}}\int \mathrm{d}M n(M)\langle N_{\mathrm{sat}}|M\rangle, \quad (18)$$

with the corresponding central fraction $f_{\mathrm{cen}} = 1 - f_{\mathrm{sat}}$.

The effective halo mass, the typical mass of galaxy host halo is

$$M_{\mathrm{eff}} = \frac{1}{n_{\mathrm{g}}}\int \mathrm{d}M M n(M)\langle N|M\rangle. \quad (19)$$

The average effective bias factor, which characterizes the clustering of galaxies relative to dark matter, is

$$b_{\mathrm{eff}} = \frac{1}{n_{\mathrm{g}}}\int \mathrm{d}M n(M) b(M)\langle N|M\rangle, \quad (20)$$

where $b(M)$ is the halo bias, a function of halo mass M. We use $b(M)$ from Tinker et al. (2010).

5.3 Fitting HOD models to HiZELS Hα-emitting galaxies

We use the HMF (Murray, Power & Robotham 2013) and HALOMOD codes (Murray 2015) to fit HOD models to the correlation functions. These take an HOD parametrization and construct real-space correlation functions for a range of parameter inputs. For each set of parameter inputs, we compare the projection of the modelled real-space correlation function with that observed, and calculate the log likelihood. We use EMCEE (Foreman-Mackey et al. 2013), a fast PYTHON implementation of an affine-invariant Markov Chain Monte

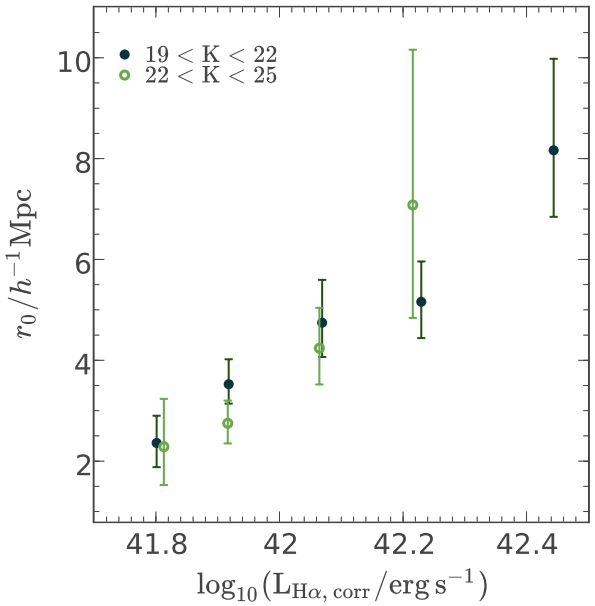

Figure 4. To investigate whether trends with $L_{H\alpha}$ are driven by stellar mass, we plot r_0 against $L_{H\alpha}$ for observed K-band magnitude-selected subsamples of the $z = 0.8$ HiZELS emitters. We find that the strong trends of clustering strength with Hα luminosity hold for these subsamples. This indicates that trends with $L_{H\alpha}$ are not driven primarily by stellar mass.

Carlo (MCMC) ensemble sampler to sample the parameter space of our five fitted parameters and optimize the fit to the correlation function. As discussed, we fit the number density of galaxies in the log-likelihood fitting as a further constraint. We use 500 walkers, each with 1000 steps.

We present examples of the best-fitting modelled correlation function and its HOD occupation, decomposed into the central and satellite galaxy terms, in Fig. 5. The parametrization, shown here for a correlation function constructed using the full sample of galaxies at $z = 0.8$, provides a good fit to the data, and clearly shows the separate contributions of the clustering within a single halo and between dark matter haloes.

For each correlation function to which an HOD model is fitted, we estimate the following parameters: f_{sat}, M_{eff}, b_{eff}, M_{min}. We take the 50th, 16th and 84th percentiles of the posterior distribution of each of these derived parameters to obtain an estimate of the median and associated 1σ errors. The individual HOD input parameters $\sigma_{\log M}$, $F_c^{A,B}$ and F_s tend to be individually less well constrained due to correlations between them. In Table 5, we present the five HOD parameters fitted to the correlation functions of large samples of galaxies within a fixed $L_{H\alpha}/L^*_{H\alpha}$ range at each redshift. In Appendix B3, we show an example of the MCMC output for one of our HOD fits.

The selection of galaxies within a fixed $L_{H\alpha}/L^*_{H\alpha}$ range, as in Section 4.1 (see Table 4), allows the comparison of similar galaxies across cosmic time. Interestingly, the derived galaxy occupations as a function of halo mass are similar, consistent within their errors (see Fig. 6). Although the $L_{H\alpha}/L^*_{H\alpha}$ distributions are not exactly the same across the different redshift ranges, we deduce from this that samples of galaxies selected from HiZELS at similar $L_{H\alpha}/L^*_{H\alpha}$ trace similar dark matter haloes across redshift. Intrigued by this, we compare galaxies within narrower $L_{H\alpha}/L^*_{H\alpha}$ bins in Section 5.4.

5.4 Luminosity dependence of HOD models

Before extending the HOD analysis to Hα luminosity-binned data at all three redshifts, we show fits to luminosity-binned and luminosity-limited data at a single epoch, $z = 0.8$, where we have

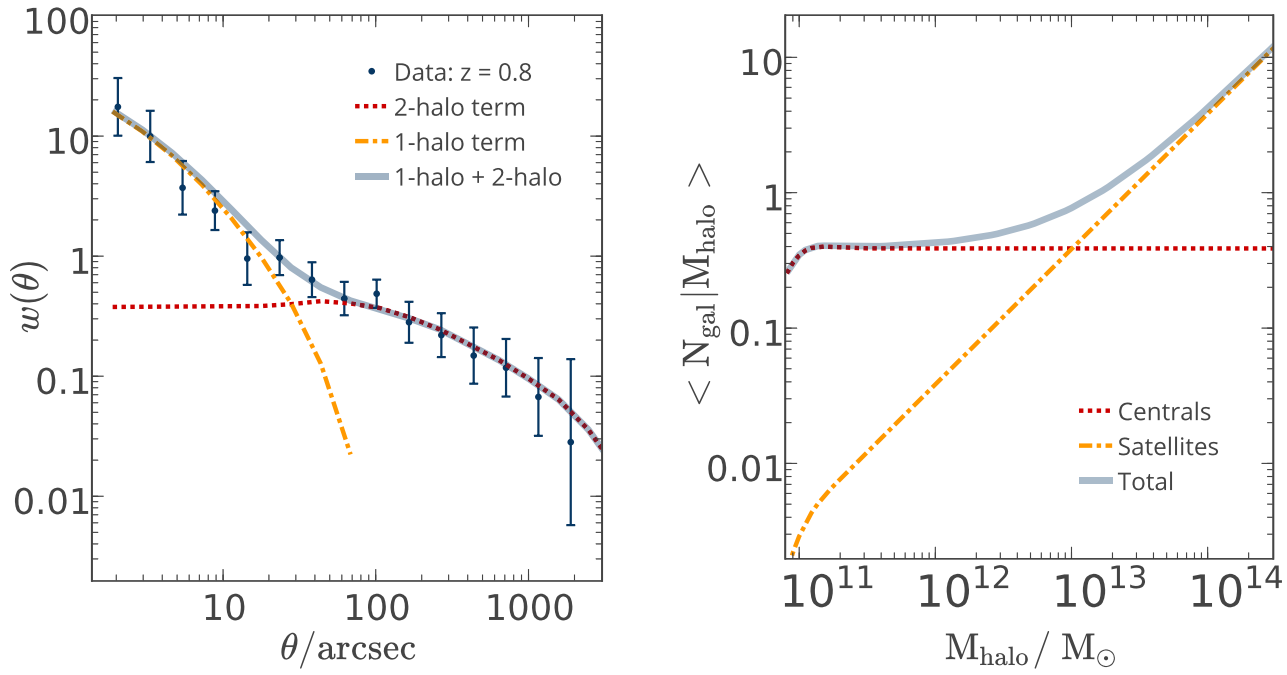

Figure 5. Left: halo occupation model fit to the correlation function of the whole $z = 0.8$ sample using HALOMOD. This multiparameter model provides a better fit to data than the single power-law model and shows the separate contributions of satellite and central galaxies. Right: the best-fitting HOD model. The contribution from satellite galaxies becomes significant only in haloes more massive than $\sim 10^{13}\,M_\odot$.

Table 5. Fitted HOD parameters, with MCMC priors used (form, minimum, maximum, starting point). We show here the derived parameters for the large samples of galaxies within a fixed $L_{\mathrm{H}\alpha}/L^*_{\mathrm{H}\alpha}$ range at each redshift. M_{min} is the minimum mass halo hosting a galaxy, F_s determines the number of satellite galaxies per halo, $F_c^{A,B}$ are normalization factors and σ is the width of the Gaussian distribution of centrals around its peak, M_{min}.

Redshift	$\log_{10}(M_{\mathrm{min}}/\mathrm{M}_\odot)$	F_s	F_c^A	F_c^B	σ
	['unif', 10, 13.0, 11.5]	['unif', 0.001, 1.0, 0.01]	['unif', 0.001, 1.0, 0.9]	['unif', 0.001, 1.0, 0.4]	['log', 0.05, 1.0, 0.5]
0.8	$11.08^{+0.12}_{-0.15}$	$0.002^{+0.001}_{-0.001}$	$0.3^{+0.2}_{-0.3}$	$0.6^{+0.3}_{-0.3}$	$0.5^{+0.3}_{-0.2}$
1.47	$11.45^{+0.06}_{-0.08}$	$0.005^{+0.003}_{-0.002}$	$0.7^{+0.2}_{-0.4}$	$0.7^{+0.3}_{-0.4}$	$0.6^{+0.3}_{-0.3}$
2.23	$11.40^{+0.06}_{-0.07}$	$0.007^{+0.003}_{-0.003}$	$0.7^{+0.2}_{-0.4}$	$0.6^{+0.3}_{-0.4}$	$0.6^{+0.3}_{-0.4}$

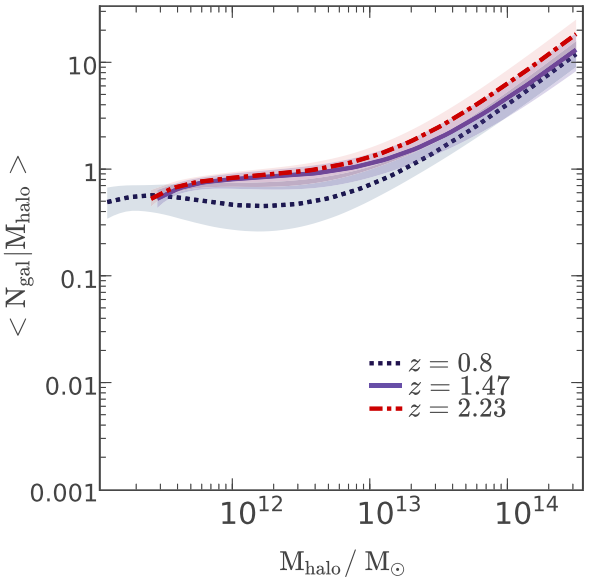

Figure 6. HOD parametrizations of samples of galaxies at $z = 0.8$, 1.47 and 2.23, within fixed ranges of $L_{\mathrm{H}\alpha}/L^*_{\mathrm{H}\alpha}$ line up closely. Although the $L_{\mathrm{H}\alpha}/L^*_{\mathrm{H}\alpha}$ distributions are not exactly the same across the different redshift ranges, galaxies selected at similar $L_{\mathrm{H}\alpha}/L^*_{\mathrm{H}\alpha}$ seem to trace similar dark matter haloes across redshift.

the largest and most robust sample (Fig. 7). For the highest luminosity (SFR) bins (e.g. dark blue line), there is a clear shift towards the right, indicating that galaxies typically occupy higher mass dark matter haloes with increasing Hα luminosity. The lowest luminosity bin (yellow line) is also interesting: the central galaxy distribution is strongly peaked around $M_{\mathrm{halo}} \sim 10^{11}\,\mathrm{M}_\odot$. Therefore, high-mass haloes do not tend to host central galaxies with these low SFRs.

The luminosity-binned and luminosity-limited results are largely self-consistent, though there is some discrepancy between the sum of the HODs of independent luminosity bins (black line) and the HOD of the sum of the luminosity bins (grey). This is particularly evident at halo masses in the range of $10^{12}\,\mathrm{M}_\odot < M_{\mathrm{halo}} < 10^{13}\,\mathrm{M}_\odot$, where the bins sum to more than one central galaxy per halo. We attribute this to the limitations of our parametrization and to the uncertainties inherent in fitting HODs to correlation functions constructed using limited numbers of galaxies.

The luminosity-limited HODs broadly agree with the halo occupation of simulated Hα emitters from the semi-analytic model GALFORM. Geach et al. (2012) show the HOD of GALFORM emitters with $L_{\mathrm{H}\alpha} > 10^{42}\,\mathrm{erg\,s^{-1}}$, which is in excellent agreement with our derived HOD (the right-hand panel of Fig. 7, green line). Both HODs show the occupation of central galaxies peaking at $M_{\mathrm{halo}} \sim 10^{12}\,\mathrm{M}_\odot$, with satellites becoming dominant at $M_{\mathrm{halo}} \sim 10^{13}\,\mathrm{M}_\odot$. HODs derived from the highest luminosity GALFORM sources display a dip in the occupation of haloes around $10^{13}\,\mathrm{M}_\odot$, with high-mass haloes in GALFORM preferentially hosting low-luminosity galaxies. We see no evidence for this, but do not reach the high luminosities of $L_{\mathrm{H}\alpha} > 10^{43}\,\mathrm{erg\,s^{-1}}$, where this is most clear in the simulated galaxies. We now explore these trends in greater detail using binned samples at all three redshifts.

At all three redshifts, we observe strong trends in the derived HOD parameters with galaxy Hα luminosity (left-hand panels of Fig. 8, see also Table 4). The effective bias, which characterizes the increased clustering of galaxies compared to dark matter, increases roughly linearly with Hα luminosity: more highly star-forming galaxies are therefore more strongly clustered with respect to the underlying dark matter distribution. The effective bias also increases towards higher redshifts. This reflects the growth of the dark matter correlation function with time (Weinberg et al. 2004). The first galaxies to form – those at high redshift – are more biased relative to the underlying mass distribution that itself is less strongly clustered.

The effective mass (M_{eff}) is the average mass of the dark matter halo inhabited by the star-forming galaxies in our samples. The relationship between effective mass of the host dark matter haloes and Hα luminosity is similar to that of the bias: galaxies with higher SFR lie, on average, in more massive dark matter haloes. At fixed Hα luminosity, the dark matter halo mass increases steeply towards low redshifts. The minimum mass of dark matter halo that hosts star-forming galaxies scales with Hα luminosity in a similar way: more luminous satellite galaxies are hosted by more massive dark matter haloes.

To compare similar populations of galaxies at the three different redshifts, we scale by the characteristic luminosity once again (see the right-hand panels of Fig. 8). Values of M_{min} from samples at all three redshifts form a tight sequence when plotted against $\log_{10}(L_{\mathrm{H}\alpha}/L^*_{\mathrm{H}\alpha})$. This is key: if we select galaxies at a given luminosity relative to the characteristic luminosity at any redshift, they reside in dark matter haloes of the same minimum mass. M_{eff} shows a similar, broadly redshift-independent trend, though there is tentative evidence of evolution to slightly higher masses towards lower redshifts, as the mass of typical dark matter haloes grows with cosmic time. We obtain the following best-fitting relations by fitting to one set of bins at each redshift:

$$\log_{10}(M_{\mathrm{min}}/\mathrm{M}_\odot) = (1.64 \pm 0.11)\,\log_{10}\left(L_{\mathrm{H}\alpha}/L^*_{\mathrm{H}\alpha}\right) + (11.94 \pm 0.02) \quad (21)$$

$$\log_{10}(M_{\mathrm{eff}}/\mathrm{M}_\odot) = (1.40 \pm 0.12)\,\log_{10}\left(L_{\mathrm{H}\alpha}/L^*_{\mathrm{H}\alpha}\right) + (12.46 \pm 0.02). \quad (22)$$

We test for evolution in the normalization of these lines by fixing their gradients to those fitted above (1.64 and 1.40) and fitting the

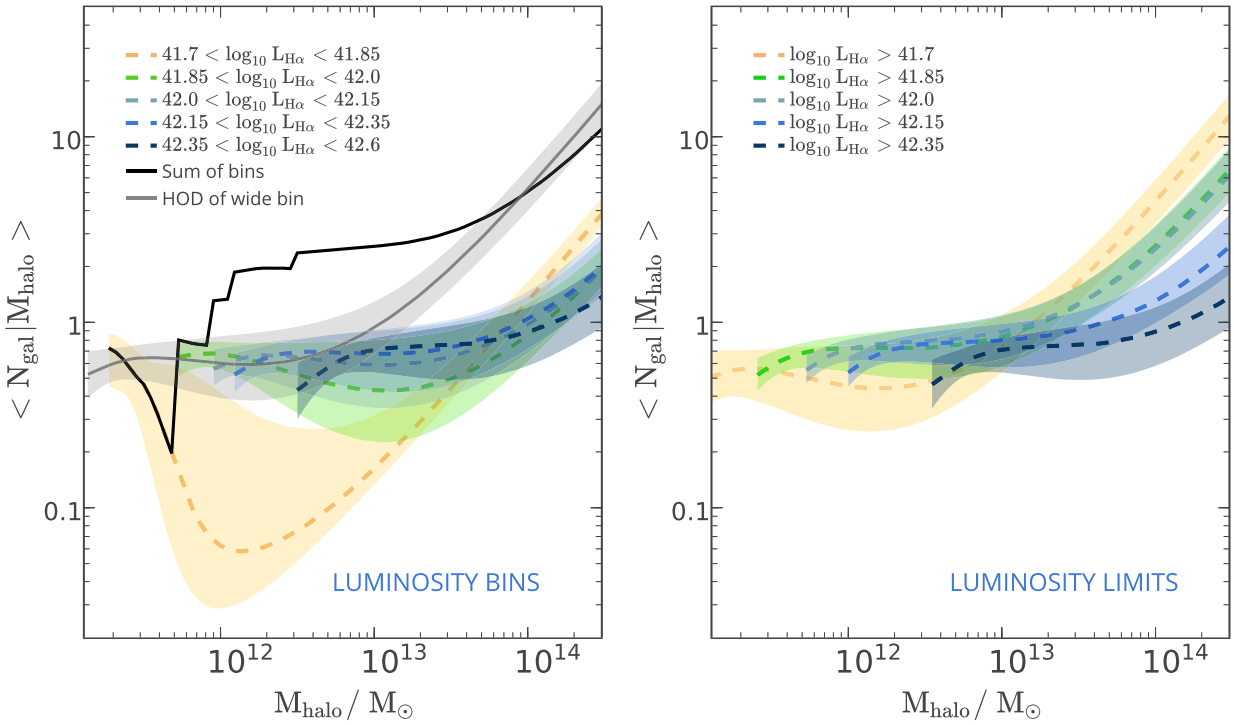

Figure 7. Fitted HODs for Hα luminosity-binned (left) and luminosity-limited (right) samples at $z \sim 0.8$. Higher luminosity Hα emitters occupy higher mass dark matter haloes. Our results are qualitatively consistent between the luminosity-binned and luminosity-limited samples, but trends are cleaner for the luminosity-limited samples, which are larger.

intercept at each redshift individually. We find intercepts of 11.92 $\pm$ 0.05 at $z = 0.8$, 11.96 $\pm$ 0.06 at $z = 1.47$ and 11.94 $\pm$ 0.08 at $z = 2.23$ for the $M_{\rm min}$ fit. Similarly, we obtain 12.54 $\pm$ 0.04 at $z = 0.8$, 12.41 $\pm$ 0.06 at $z = 1.47$ and 12.36 $\pm$ 0.06 at $z = 2.23$ for the $M_{\rm eff}$ fit. The fits are consistent to within 0.04 dex for $M_{\rm min}$ and 0.2 dex for $M_{\rm eff}$.

The satellite fraction for the HiZELS samples is the least well constrained derived parameter. This is because when a halo contains only one star-forming galaxy, the two-point correlation function cannot distinguish whether this is a central galaxy or a satellite of a central quenched galaxy. Satellite galaxies are only constrained by the one-halo term in the most massive haloes, and thus the determination of $f_{\rm sat}$ is sensitive to the form of the HOD parametrization (which extrapolates this to lower masses). Nevertheless, we find no evidence of a change in satellite fraction with redshift with luminosity or with redshift (Fig. 9). As noted previously, this satellite fraction is only the fraction of *star-forming satellites in the sample*, and may be higher if passive populations were included. There is a slight indication of an upturn in satellite fractions at the highest luminosities, but at low significance. Fig. 7 had shown that the sum of the HODs of luminosity-binned samples clearly exceeds the HOD of the whole sample at moderate halo masses of $M_{\rm halo} \sim 10^{12}$–$10^{13}\,{\rm M}_{\odot}$ by a factor of $\sim$2. This suggests that the HOD fits to luminosity-binned samples are overestimating the number of central galaxies in the sample. This would decrease the satellite fraction and explain the discrepancy between the $\sim$5 per cent satellite fractions derived for the whole samples (see Table 4) and those of luminosity-binned samples, which stand at $\sim$3 per cent. The $\sim$5 per cent satellite fraction is likely to be closer to the 'true' satellite fractions of our samples. Nevertheless, the main result of Fig. 9 is that there is no evidence that $f_{\rm sat}$ changes dramatically with either $L_{\rm H\alpha}$ or redshift.

Finally, we note that when scaled by $L^*_{\rm H\alpha}$, the luminosity–bias relations show strong redshift dependence. This is due to the growth of the dark matter correlation function with time. The different redshifts align better in the $\log_{10}L_{\rm H\alpha}$ versus bias plot, but this is likely to be simply because at fixed $L_{\rm H\alpha}$, selection of brighter (relative to $L^*_{\rm H\alpha}$) galaxies at low redshift goes some way towards compensating the dark matter halo growth.

6 DISCUSSION

Having studied the halo environments of galaxies at three different redshifts, we draw together the main findings here. The Hα-selected galaxies detected by the HiZELS survey are typical star-forming galaxies that reside in dark matter haloes of masses $\sim 10^{12}\,{\rm M}_{\odot}$. Our typical HiZELS-limiting Hα fluxes correspond to SFRs of $\sim$4 ${\rm M}_{\odot}\,{\rm yr}^{-1}$ at $z = 0.8$, $\sim$8 ${\rm M}_{\odot}\,{\rm yr}^{-1}$ at $z = 1.47$ and $\sim$13 ${\rm M}_{\odot}\,{\rm yr}^{-1}$ at $z = 2.23$, according to the Hα-SFR conversion of Kennicutt (1998). At all redshifts, in all luminosity bins, we find low satellite fractions of $\sim$5 per cent, with fitted HODs only reaching above one star-forming satellite per halo in haloes of $\geq 10^{13}\,{\rm M}_{\odot}$. Whilst there are some uncertainties introduced by the limitations of our HOD parametrization, the satellite fractions derived are consistently low for both luminosity-limited and luminosity-binned samples of Hα emitters. We conclude that the majority of the star-forming galaxies in our samples are centrals.

The star-forming galaxies detected at lower redshifts ($z = 0.8$ and 1.47) have lower Hα luminosities than the high-redshift $z = 2.23$ galaxies that reside in equally massive haloes. This reflects the general trend of decreasing SFR towards low redshift (see Daddi et al. 2007; Elbaz et al. 2007; Karim et al. 2011; Sobral et al. 2014; Lee et al. 2015). At all three redshifts, we find an increase in estimated average host dark matter halo mass with Hα luminosity

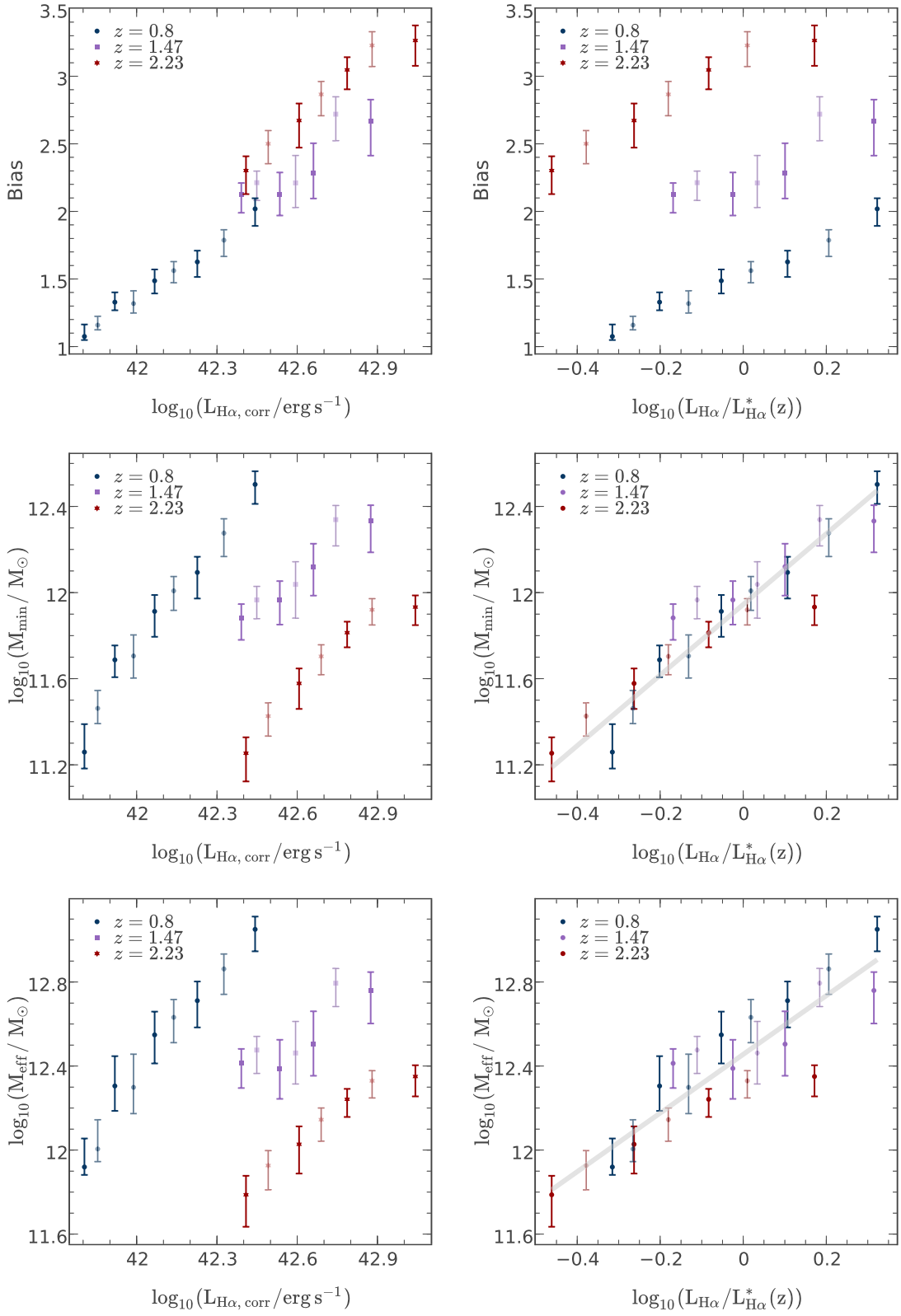

Figure 8. Derived properties of galaxy populations of HiZELS galaxies binned by Hα luminosity. We find a linear, broadly redshift-independent relationship between halo mass and Hα luminosity. As in Fig. 3, the paler colours denote alternative binning. The lines of best fit derived in Section 5.4 are overplotted: $\log_{10}(M_{\rm min}/{\rm M}_{\odot}) = (1.64 \pm 0.11)\log_{10}(L_{{\rm H}\alpha}/L^{*}_{{\rm H}\alpha}) + (11.94 \pm 0.02)$, $\log_{10}(M_{\rm eff}/{\rm M}_{\odot}) = (1.40 \pm 0.12)\ \log_{10}(L_{{\rm H}\alpha}/L^{*}_{{\rm H}\alpha}) + (12.46 \pm 0.02)$.

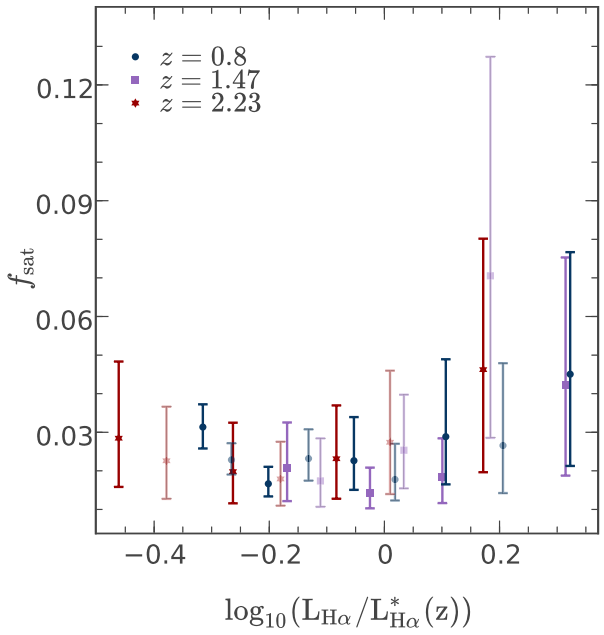

Figure 9. The derived satellite fraction is low for all redshifts and luminosity bins, indicating that HiZELS galaxies are primarily centrals. However, the satellite fraction is the least well constrained of the HOD output parameters. Again, the paler colours denote alternative binning.

of galaxies studied. More highly star-forming galaxies are hosted by more massive dark matter haloes.

We emphasize here that we have performed the analysis on a sample of galaxies selected cleanly by Hα emission line strength. These galaxies are predominantly star forming, with luminosities close to the characteristic luminosity at each redshift, and are therefore representative of the star-forming population (Oteo et al. 2015). If we were to probe down to much lower SFR (including the passive galaxy population), trends in halo mass versus Hα luminosity may eventually reverse. Hartley et al. (2010), for example, found passive galaxies to be significantly more strongly clustered than their star-forming counterparts back to $z \sim 2$ (see also Wilkinson et al. 2017). This fits easily into our interpretation: the passive, massive galaxies at a given redshift formed their mass early (downsizing; Cowie et al. 1996), and hence quickly. Indeed, we find that the most highly star-forming galaxies at all redshifts are the most strongly clustered.

6.1 The halo mass–characteristic luminosity relation

Scaling by the characteristic luminosity at each redshift enables us to compare similar populations of galaxies. The $\log_{10}(L_{\mathrm{H}\alpha}/L^*_{\mathrm{H}\alpha})$ versus halo mass relations line up very tightly, and as shown in Fig. 4, this is a genuine trend, not driven by stellar mass. This indicates that the mass of the host dark matter halo is driving the typical luminosity of its star-forming galaxies. The minimum halo mass at $L_{\mathrm{H}\alpha} = L^*_{\mathrm{H}\alpha}$ is $\sim 10^{12}\,\mathrm{M}_\odot$ for all three redshifts. This exactly coincides with the peak of the stellar mass–halo mass relation (SHMR), the halo mass at which the star formation efficiency peaks, within this redshift range (Behroozi, Conroy & Wechsler 2010; Behroozi, Wechsler & Conroy 2013). As noted by Behroozi et al. (2013), the halo mass at which the SHMR is at its maximum is also that at which the baryon conversion efficiency (the ratio of the SFR to the halo's baryon accretion rate) is highest. Models predict that this holds across a large redshift range, until at least $z = 4$. Our results support the conclusion that haloes of mass $\sim 10^{12}\,\mathrm{M}_\odot$ are the most efficient at forming stars at every epoch. The SHMR decreases at higher halo masses, which are less efficient at forming stars. We obtain $M_{\rm min} \sim 10^{12\text{–}12.4}\,\mathrm{M}_\odot$ for our most luminous galaxies, in line with this. This is consistent with the models of Dekel & Birnboim (2006), which posit a roughly redshift-independent limiting halo mass of $M_{\rm shock} \sim 10^{12}\,\mathrm{M}_\odot$, above which efficient gas cooling is prevented by shock heating. Sobral et al. (2016a) find that those HiZELS galaxies with $L_{\mathrm{H}\alpha} > L^*_{\mathrm{H}\alpha}$ have increasing AGN fractions, whilst Sobral et al. (2009) find that these very luminous galaxies are much more likely to be mergers than their low-luminosity counterparts (the fraction of $z = 0.84$ HiZELS galaxies with irregular morphologies increases from <20 per cent below $L_{\mathrm{H}\alpha} = L^*_{\mathrm{H}\alpha}$ to ∼100 per cent at $L_{\mathrm{H}\alpha} > L^*_{\mathrm{H}\alpha}$). This supports the argument that $L^*_{\mathrm{H}\alpha}$ is the luminosity where 'normal', non-merger-driven star formation peaks.

6.2 Interpretation via an equilibrium gas-regulator model

In this section, we use a few simple ideas from models of the evolution of galaxies and dark matter haloes to link the luminosities of the star-forming galaxies in our sample to the growth of dark matter haloes over cosmic time.

Fakhouri, Ma & Boylan-Kolchin (2010) derive the mean halo mass growth as a function of mass and redshift, using the Millennium simulation:

$$\left\langle \frac{\mathrm{d}m_{\rm halo}}{\mathrm{d}t} \right\rangle = 46.1 \left(\frac{m_{\rm halo}}{10^{12}}\right)^{1.1} (1 + 1.11z)\sqrt{\Omega_{\rm M}(1+z)^3 + \Omega_\Lambda}. \tag{23}$$

We gather the terms $(1 + 1.11z)\sqrt{\Omega_{\rm M}(1+z)^3 + \Omega_\Lambda}$ and call them $f(z)$ from here onwards.

We define the halo specific mass inflow rate, $\mathrm{sMIR}_{\rm DM}$, as

$$\mathrm{sMIR}_{\rm DM} = \frac{1}{m_{\rm halo}} \frac{\mathrm{d}m_{\rm halo}}{\mathrm{d}t}. \tag{24}$$

We now attempt to relate this to star formation in galaxies. Equilibrium models, in which star formation in a galaxy is regulated by the instantaneous mass of gas in its reservoir and mass-loss is similarly regulated by the SFR, have been successful in reproducing many observed galaxy properties including gas fractions and metallicities to $z \sim 2$ (e.g. Davé, Finlator & Oppenheimer 2012; Lilly et al. 2013; Saintonge et al. 2013). In the gas-regulated model of galaxy evolution proposed by Lilly et al. (2013), the specific star formation rate (sSFR) of a central galaxy is related to the average specific mass accretion rate of its dark matter halo via:

$$\mathrm{sSFR} = \frac{1}{(1-\eta)(1-R)} \mathrm{sMIR}_{\rm DM}, \tag{25}$$

where η (the slope of the mass–metallicity relation) and R (which determines the fraction of stars that are long-lived) are observationally determined constants.

Substituting $\mathrm{sSFR} = \mathrm{SFR}/m_{\rm star}$, and using $\mathrm{SFR} = 7.9 \times 10^{-42} L_{\mathrm{H}\alpha}$, from Kennicutt (1998), then combining equations (23) and (24) yields

$$L_{\mathrm{H}\alpha} = k\, m_{\rm halo}^{0.1}\, m_{\rm star}\, f(z), \tag{26}$$

where k is a numerical factor.

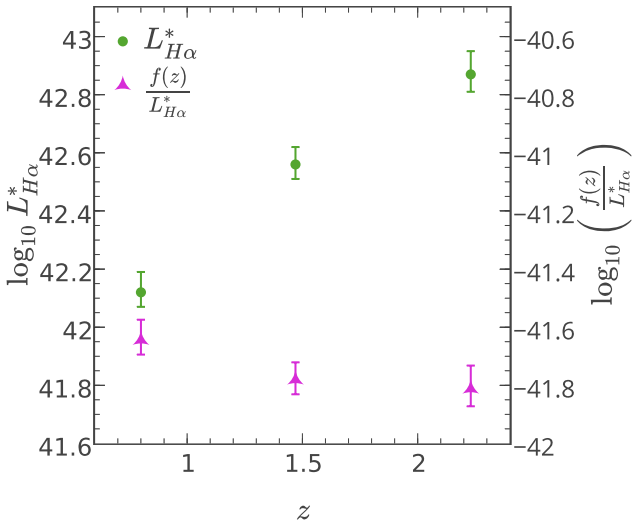

Figure 10. The characteristic Hα luminosity, $L^*_{\mathrm{H}\alpha}$, displays a striking increase with redshift. Once scaled by the halo mass growth factor, $f(z)$, from Fakhouri et al. (2010), we observe little evolution. This indicates that the evolution in $L^*_{\mathrm{H}\alpha}$, and therefore in the star formation history of the universe, is driven by dark matter halo mass accretion.

We found in Section 5.4 that the scaled mean Hα luminosity, $L_{\mathrm{H}\alpha}/L^*_{\mathrm{H}\alpha}$, of a sample of our star-forming galaxies is related to halo mass in a redshift-independent manner:

$$\frac{L_{\mathrm{H}\alpha}}{L^*_{\mathrm{H}\alpha}(z)} \approx \left(\frac{m_{\mathrm{halo}}}{10^{12}}\right)^{1/1.6}. \quad (27)$$

Dividing equation (26) by $L^*_{\mathrm{H}\alpha}$, we obtain

$$\frac{L_{\mathrm{H}\alpha}}{L^*_{\mathrm{H}\alpha}(z)} \approx k\, m_{\mathrm{halo}}^{0.1}\, m_{\mathrm{star}}\, \frac{f(z)}{L^*_{\mathrm{H}\alpha}(z)}, \quad (28)$$

which from our observed relation (equation 27) must remain constant with redshift for a given m_{halo}.

The average galaxy stellar mass, m_{star}, is also related to m_{halo} broadly independently of redshift within our range of redshifts (the SHMR; Behroozi et al. 2013; Birrer et al. 2014; Hatfield et al. 2016). Therefore, to maintain equation (27) across cosmic time in the context of the gas-regulator model,

$$\frac{f(z)}{L^*_{\mathrm{H}\alpha}(z)} = \mathrm{const.} \quad (29)$$

must hold.

To test this, we calculate $\frac{f(z)}{L^*_{\mathrm{H}\alpha}(z)}$ for the HiZELS samples at the three different redshifts. We find that this is, indeed, fairly constant compared to the strong evolution in $L^*_{\mathrm{H}\alpha}$ (see Fig. 10). Whereas $L^*_{\mathrm{H}\alpha}$ changes by an order of magnitude, $\frac{f(z)}{L^*_{\mathrm{H}\alpha}(z)}$ changes by less than 0.2 dex. Our results therefore support a model in which the evolution in $L^*_{\mathrm{H}\alpha}$ is driven solely by the halo mass growth, in line with a gas-regulator model. We thus conclude that our HiZELS galaxies are dominated by typical star-forming galaxies in equilibrium, rather than extreme, merger-driven starburst systems, even at high redshifts. The halo mass accretion rate is the dominant driver of star formation in these galaxies across the large redshift range of $0.8 < z < 2.23$.

6.3 Satellite fractions and environmental quenching

We have found low satellite fractions (∼5 per cent) at all three of the redshifts studied, and in all luminosity bins, using this HOD parametrization. The gas-regulator model, shown in Section 6.2 to fit our observations well, does not include any satellite-specific mechanisms like ram pressure stripping. This supports the conclusion that the majority of HiZELS galaxies are centrals.

As discussed earlier, the exact values we derive for the satellite fraction may be significantly dependent on the HOD parametrization we adopted, as two-halo clustering cannot discriminate between centrals and satellites. Nevertheless, it is possible to demonstrate that the satellite fraction must be low. Many HOD models of mass-selected samples of galaxies (including at these redshifts; e.g. Wake et al. 2011; Hatfield et al. 2016) use a power-law satellite occupancy model with $\alpha \approx 1$, with a low-mass cut-off below halo mass $\sim 10^{13}\,\mathrm{M}_\odot$. As shown in our HOD modelling, obtaining a good fit to our (relatively low-amplitude) correlation functions requires a substantial contribution from low-mass haloes, down to $<10^{12}\,\mathrm{M}_\odot$. The scarcity of satellites in these low-mass haloes, coupled with the increase in the halo mass function at low halo masses, thus mandates a fairly low overall satellite fraction. To quantify this, we consider a conservative model in which the satellite occupancy of haloes follows a power law with $\alpha = 1$ down to the lowest masses (i.e. no cut-off), normalized to unity at $M_{\mathrm{halo}} = 2 \times 10^{13}\,\mathrm{M}_\odot$ (cf. Wake et al. 2011; Hatfield et al. 2016). Even if all potential satellite galaxies were to be star forming, our total HOD model for the 'full' sample at $z = 0.8$ then permits a maximum satellite fraction of ∼8 per cent (this increases to ∼14 per cent for a normalization of $<N_{\mathrm{sat}}|M> = 1$ at $M_{\mathrm{halo}} = 10^{13}\,\mathrm{M}_\odot$). We can thus safely conclude that satellite fractions must be low.

Detailed comparison of our HOD modelling result with those of mass-selected samples at these same redshifts would require us to match the samples in stellar mass; this is beyond the scope of this paper. Nevertheless, we can gain some initial insights by comparison with the results of Hatfield et al. (2016), who studied mass-selected samples in a similar stellar mass range as our Hα emitters, in overlapping redshift ranges, using the same HOD fitting code as ours (thus minimizing any systematic errors). Hatfield et al. (2016) find satellite fractions of $\sim 13 \pm 1$ per cent at $z \sim 0.8$ and $\sim 6 \pm 1$ per cent at $z \sim 1.5$, integrating down to the lowest galaxy stellar masses within their samples. Our redshift-independent satellite fraction of star-forming galaxies, when compared to the increasing satellite fraction amongst mass-selected galaxies towards low redshift, indicates that a significantly larger portion of satellites are star-forming at higher redshifts. These results are consistent with those of Tal et al. (2014), who find that the quiescent fraction for satellites increases towards low redshift, from ∼10 per cent at $z \sim 1.5$ to ∼30 per cent at $z \sim 0.8$, with onset of satellite quenching taking place several giga years after the first centrals reach quiescence.

Our results may also provide insights into the quenching mechanisms acting at high redshifts. A number of studies find a strong excess of starbursting submm galaxies in high-redshift cluster environments (Elbaz et al. 2007; Smail et al. 2014; Ma et al. 2015). In some cases, these starbursting galaxies reside in the cluster core (e.g. Ma et al. 2015), and in others, they lie towards the cluster's outskirts, with passive galaxies dominating the central regions (e.g. Smail et al. 2014). If this intense star formation were driven by an enhanced intracluster gas supply, we would expect to see enhanced star formation throughout these high-mass haloes, reflected in high satellite fractions and increased effective halo masses for our HiZELS galaxies at higher redshifts. Instead, we find that both

of these properties remain broadly consistent. Combined with the submm view, our results support the scenario put forward by McGee et al. (2009), in which upon infall on to a rich cluster, compression of high gas contents within galaxies may provoke intense, dust-obscured star formation, after which quenching proceeds on fairly long time-scales (>2 yr) via gas stripping or exhaustion.

7 CONCLUSIONS

We have used HiZELS galaxies selected by the strength of their Hα emission to study the clustering of star-forming galaxies at three well-defined epochs: $z = 0.8$, 1.47 and 2.23. Our samples comprise typical star-forming galaxies on and just above the 'main sequence' at each redshift. We have constructed two-point correlation functions and fitted these with simple power-law fits, finding that the clustering strength, r_0, of HiZELS sources at all redshifts increases linearly with their Hα luminosity, from $r_0 \sim 2{-}3\ h^{-1}$ Mpc for the lowest luminosity sources in our samples to $r_0 \sim 7{-}8\ h^{-1}$ Mpc for the most luminous. We have demonstrated that this is not driven by galaxy stellar mass.

We then used MCMC techniques to fit the same correlation functions with a more sophisticated HOD models, deriving each galaxy population's effective bias, satellite fraction and indicative dark matter halo masses. We summarize the key results here:

(i) Typical Hα-emitting galaxies in the redshift range $z = 0.8$–2.2 are star-forming centrals, residing in host haloes of minimum mass $10^{11.2}$–$10^{12.6}$ M$_\odot$ and effective mass $10^{11.6}$–10^{13} M$_\odot$. At all three redshifts, $L^*_{\mathrm{H}\alpha}$ galaxies typically reside in haloes of mass $\sim 10^{12}$ M$_\odot$. This coincides with the halo mass predicted by theory to be maximally efficient at converting baryons into stars.

(ii) The effective bias of the galaxy populations (their clustering relative to the underlying dark matter) decreases towards lower redshifts, reflecting the increase of the clustering of dark matter with time. Similarly, typical masses of host haloes increase with time at fixed $L_{\mathrm{H}\alpha}$.

(iii) Bias increases linearly with Hα luminosity at all redshifts, indicating that the most highly star-forming galaxies thrive in higher dark matter overdensities, where a plentiful gas supply fuels high SFRs in the central galaxies.

(iv) Samples selected within the same $L_{\mathrm{H}\alpha}/L^*_{\mathrm{H}\alpha}$ range inhabit similar populations of dark matter haloes. Although the dark matter halo mass at fixed $L_{\mathrm{H}\alpha}$ varies by more than an order of magnitude across the three different redshifts, the relationship between scaled galaxy luminosity $L_{\mathrm{H}\alpha}/L^*_{\mathrm{H}\alpha}$ and dark matter halo mass is independent of redshift to within 0.04 dex in M_{min} and 0.2 dex in M_{eff}.

(v) Comparing our results to models of galaxy evolution based on gas regulation, we find that $L^*_{\mathrm{H}\alpha}$ evolves in line with average mass growth of the host dark matter haloes.

Together, these results reveal halo environment as a strong driver of galaxy SFR and the evolution of the LF over cosmic time. The central galaxies that dominate our samples evolve in equilibrium with their growing dark matter haloes, with typical sSFR directly proportional to the specific mass accretion rate of the host dark matter halo. Satellite fractions remain low ($\sim$5 per cent with the HOD parametrization we have adopted) for all samples, regardless of redshift or luminosity. This may indicate that their star formation is suppressed, particularly towards low redshifts and in high-mass dark matter haloes. This is in line with models of satellite quenching upon accretion on to a massive cluster. In a subsequent paper, we will extend this study to incorporate stellar mass, exploring the clustering of HiZELS galaxies as a function of Hα luminosity, stellar mass and redshift.

ACKNOWLEDGEMENTS

We are grateful to Steven Murray for making the HALOMOD and HMF PYTHON packages available and for extensive guidance on their use. We thank the anonymous referee for suggestions that have greatly improved this manuscript, and John Peacock and Peter Hatfield for helpful advice.

RKC acknowledges funding from an STFC studentship. PNB is grateful for support from STFC via grant ST/M0011229/1. DS acknowledges financial support from the Netherlands Organization for Scientific research (NWO) through a Veni fellowship and from Lancaster University through an Early Career Internal Grant A100679. IRS acknowledges support from STFC (ST/L00075X/1), the ERC Advanced Investigator programme DUSTYGAL 321334, and a Royal Society/Wolfson Merit Award. JPS gratefully acknowledges support from a Hintze Research Fellowship. This work is based on observations obtained using the WFCAM on the 3.8-m UKIRT, as part of the HiZELS (U/CMP/3 and U/10B/07). It also relies on observations conducted with HAWK-I on the ESO VLT, programme 086.7878.A, and observations obtained with Suprime-Cam on the Subaru Telescope (S10B-144S).

REFERENCES

Baldry I. K., Balogh M. L., Bower R. G., Glazebrook K., Nichol R. C., Bamford S. P., Budavari T., 2006, MNRAS, 373, 469
Baugh C. M., 2006, Rep. Prog. Phys., 69, 3101
Behroozi P. S., Conroy C., Wechsler R. H., 2010, ApJ, 717, 379
Behroozi P. S., Wechsler R. H., Conroy C., 2013, ApJ, 770, 57
Best P. N., Kaiser C. R., Heckman T. M., Kauffmann G., 2006, MNRAS, 368, L67
Birrer S., Lilly S., Amara A., Paranjape A., Refregier A., 2014, ApJ, 793, 12
Boselli A., Gavazzi G., 2006, PASP, 118, 517
Bower R. G., Benson A. J., Malbon R., Helly J. C., Frenk C. S., Baugh C. M., Cole S., Lacey C. G., 2006, MNRAS, 370, 645
Butcher H., Oemler A., 1978, ApJ, 219, 18
Cirasuolo M., McLure R. J., Dunlop J. S., Almaini O., Foucaud S., Simpson C., 2010, MNRAS, 401, 1166
Cole S., Lacey C. G., Baugh C. M., Frenk C. S., 2000, MNRAS, 319, 168
Contreras S., Baugh C. M., Norberg P., Padilla N., 2013, MNRAS, 432, 2717
Cowie L., Songaila A., Hu E., Cohen J., 1996, ApJ, 112, 839
Crain R. A. et al., 2015, MNRAS, 450, 1937
Croton D. J. et al., 2006, MNRAS, 365, 11
Daddi E. et al., 2007, ApJ, 670, 156
Darvish B., Mobasher B., Sobral D., Scoville N., Aragon-Calvo M., 2015, ApJ, 805, 121
Davé R., Finlator K., Oppenheimer B. D., 2012, MNRAS, 421, 98
Davis M., Efstathiou G., Frenk C. S., White S. D. M., 1985, ApJ, 292, 371
Dekel A., Birnboim Y., 2006, MNRAS, 368, 2
Dressler A., 1980, ApJ, 236, 351
Elbaz D. et al., 2007, A&A, 468, 33
Fakhouri O., Ma C. P., Boylan-Kolchin M., 2010, MNRAS, 406, 2267
Foreman-Mackey D., Price-Whelan A., Ryan G., Emily, Smith M., Barbary K., Brewer B. J., 2014, triangle.py v0.1.1 [Data set], Zenodo. Available at: http://doi.org/10.5281/zenodo.11020
Foreman-Mackey D., Hogg D. W., Lang D., Goodman J., 2013, PASP, 125, 306
Garn T., Best P. N., 2010, MNRAS, 409, 421
Garn T. et al., 2010, MNRAS, 402, 2017

Geach J. E., Smail I., Best P. N., Kurk J., Casali M., Ivison R. J., Coppin K., 2008, MNRAS, 388, 1473
Geach J. E., Sobral D., Hickox R. C., Wake D. A., Smail I., Best P. N., Baugh C. M., Stott J. P., 2012, MNRAS, 426, 679
Gomez P. L. et al., 2003, ApJ, 584, 210
Groth E. J., Peebles P., 1977, ApJ, 217, 385
Hartley W. G. et al., 2010, MNRAS, 407, 1212
Hatfield P. W., Lindsay S. N., Jarvis M. J., Hauessler B., Vaccari M., Verma A., 2016, MNRAS, 459, 2618
Ibar E. et al., 2013, MNRAS, 434, 3218
Ilbert O. et al., 2009, ApJ, 690, 1236
Karim A. et al., 2011, ApJ, 730, 61
Kashino D. et al., 2017, ApJ, preprint (arXiv:1703.08326)
Kennicutt R. C., 1998, ApJ, 498, 541
Landy S. D., Szalay A. S., 1993, ApJ, 412, 64
Larson R., 1980, MNRAS, 190, 321
Lawrence A. et al., 2007, MNRAS, 379, 1599
Lee N. et al., 2015, ApJ, 801, 80
Lewis I. et al., 2002, MNRAS, 334, 673
Lilly S. J. et al., 2007, ApJ, 172, 70
Lilly S. J., Carollo C. M., Pipino A., Renzini A., Peng Y., 2013, ApJ, 772, 119
Limber D. L., 1953, ApJ, 117, 134
Ma C.-J. et al., 2015, ApJ, 806, 257
McGee S. L., Balogh M. L., Bower R. G., Font A. S., McCarthy I. G., 2009, MNRAS, 400, 937
Murray S., Power C., Robotham A., 2013, Astron. Comput., 3, 23
Murray S. G., 2015, PhD thesis, Univ. of Galsgow
Muzzin A. et al., 2012, ApJ, 746, 188
Norberg P. et al., 2001, MNRAS, 328, 64
Norberg P., Baugh C. M., Gaztañaga E., Croton D. J., 2009, MNRAS, 396, 19
Oemler A., 1977, Highlights Astron., 4, 253
Oteo I., Sobral D., Ivison R. J., Chandra X.-R., 2015, MNRAS, 452, 2018
Peacock J. A., Smith R. E., 2000, MNRAS, 318, 1144
Peebles P., 1982, ApJ, 263, L1
Peng Y., Maiolino R., Cochrane R., 2015, Nature, 521, 192
Peng Y.-j. et al., 2010, ApJ, 721, 193
Peng Y.-j., Lilly S. J., Renzini A., Carollo M., 2012, ApJ, 757, 4
Saintonge A. et al., 2013, ApJ, 778, 2
Schaye J. et al., 2015, MNRAS, 446, 521
Scoville N. et al., 2013, ApJS, 206, 3
Simon P., 2007, A&A, 473, 711
Smail I. et al., 2014, ApJ, 782, 19
Sobral D. et al., 2009, MNRAS, 398, 75
Sobral D., Best P. N., Geach J. E., Smail I., Cirasuolo M., Garn T., Dalton G. B., Kurk J., 2010, MNRAS, 1563, 1551
Sobral D., Best P. N., Smail I., Geach J. E., Cirasuolo M., Garn T., Dalton G. B., 2011, MNRAS, 411, 675
Sobral D., Best P. N., Matsuda Y., Smail I., Geach J. E., Cirasuolo M., 2012, MNRAS, 420, 1926
Sobral D., Smail I., Best P. N., Geach J. E., Matsuda Y., Stott J. P., Cirasuolo M., Kurk J., 2013, MNRAS, 428, 1128
Sobral D., Best P. N., Smail I., Mobasher B., Stott J., Nisbet D., 2014, MNRAS, 427, 3516
Sobral D. et al., 2015, MNRAS, 451, 2303
Sobral D., Kohn S. A., Best P. N., Smail I., Harrison C. M., Stott J., Calhau J., Matthee J., 2016a, MNRAS, 457, 1739
Sobral D., Stroe A., Koyama Y., Darvish B., Calhau J., Afonso A., Kodama T., Nakata F., 2016b, MNRAS, 458, 3443
Springel V. et al., 2005, Nature, 435, 629
Stott J. P. et al., 2016, MNRAS, 457, 1888
Tacconi L. J., Genzel R., Neri R., Cox P., Cooper M. C., Shapiro K., Bolatto A., 2010, Nature, 463, 781
Tal T. et al., 2014, ApJ, 789, 164
Tinker J. L., Robertson B. E., Kravtsov A. V., Klypin A., Warren M. S., Yepes G., Gottlöber S., 2010, ApJ, 724, 878
Vogelsberger M. et al., 2014, Nature, 509, 177
Wake D. A. et al., 2011, ApJ, 728, 46
Weinberg D. H., Dave R., Katz N., Hernquist L., 2004, ApJ, 601, 1
White S. D. M., Frenk C. S., 1991, ApJ, 379, 52
Wilkinson A. et al., 2017, MNRAS, 464, 1380
York D., Adelman J., 2000, ApJ, 120, 1579
Zehavi I. et al., 2005, ApJ, 630, 1
Zehavi I. et al., 2011, ApJ, 736, 59
Zheng Z. et al., 2005, ApJ, 633, 791
Zwicky F., 1933, Helv. Phys. Acta, 6, 110

APPENDIX A: CORRELATION FUNCTION FITS

In Section 4, we calculate correlation functions in bins of Hα luminosity and show the resultant r_0 values in Fig. 4. For the $z = 0.8$ samples, we show examples of the quality of the correlation functions constructed from luminosity-binned samples in Fig. A1.

APPENDIX B: FURTHER DETAILS ON HOD PARAMETRIZATIONS AND FITS

B1 Choosing an HOD parametrization

We have fitted a typical HiZELS correlation function (generated using the whole sample at $z = 0.8$) using four different HOD parametrizations that have been proposed for SFR-limited samples (see Section 5.3 for more details of the fitting procedure). The parametrizations are as follows: the full eight-parameter model described in Section 5.1; the five-parameter model adopted by Geach et al. (2012); a six-parameter model that is identical to the five-parameter model apart from fitting α as a further parameter; and the five-parameter model of Zheng et al. (2005), frequently used for mass-selected samples. We truncate all parametrizations at the lower limit $M_{\rm min}$. We show in Fig. B1 that these parametrizations all do well at fitting the data. Derived quantities are given in Table B1. It is important to note that the derived quantities, $b_{\rm eff}$, $M_{\rm eff}$, $f_{\rm sat}$ and

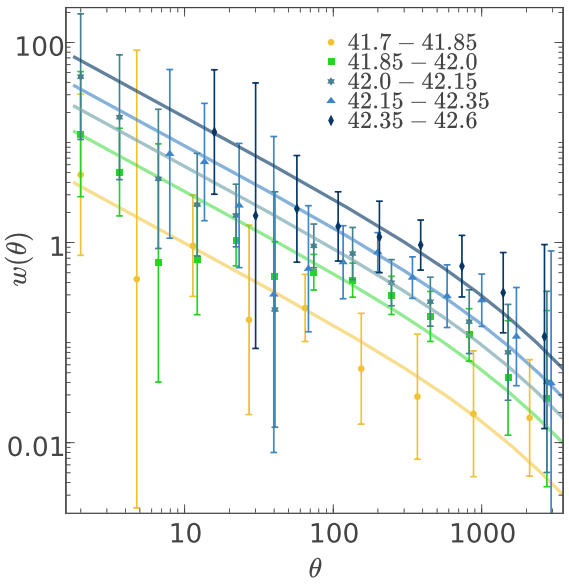

Figure A1. Examples of five correlation functions of luminosity-binned samples at $z = 0.8$. Although the correlation functions are not as high quality as those of the whole samples (e.g. Fig. 3), it is clear that the clustering strength (obtained from the amplitude of the correlation function) increases with $L_{\rm H\alpha}$ luminosity.

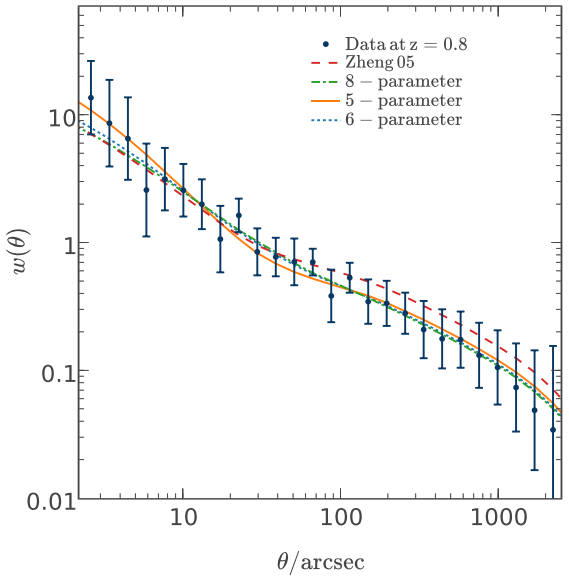

Figure B1. Comparison of best-fitting correlation functions derived using different HOD parametrizations. We adopt the five-parameter Geach et al. (2012) parametrization as it fits the correlation function well on all scales and additional parameters are not justified by any improvement to the fit. We truncate all parametrizations, using a lower integral limit of M_{min}.

M_{min} are fairly consistent between parametrizations, and the choice of parametrization does not substantially alter the conclusions of this paper.

We conclude that the truncated five-parameter HOD of Geach et al. (2012) provides a sufficiently good reproduction of the correlation function. Higher order parametrizations are not justified by improvements in the fit to the correlation function. With the smaller sizes of luminosity-binned samples, minimizing the number of free parameters is important to obtain good parameter constraints, and so we adopt the five-parameter approach. We emphasize that we also checked our analyses with the six-parameter model (allowing α to vary), and recovered consistent results, also finding $\alpha \approx 1$.

B2 Testing the lower limit on the HOD integral

If the halo occupation numbers fall steeply at low halo masses, we can safely set the lower limit of the integral at an arbitrary, low halo mass. In practice, we find that fits to our correlation functions produce poorly defined Gaussian peaks, with fairly flat occupations at low masses (see Section 5.4). To test different lower limits here, we integrate to fixed distances (0, 0.25, 0.5 and 1 dex) below M_{min} during the HOD fitting process. We perform this test for two different correlation functions, constructed using $z \sim 0.8$ sources in two luminosity bins. The best-fitting HODs for each trial are shown in Fig. B2. The fitted values of σ tend to be large and highly correlated

Table B1. Derived parameters from fitting the whole sample at $z \sim 0.8$ with for four different halo model parametrizations. The values of these derived parameters depend little on the choice of parametrization.

Parametrization	b_{eff}	M_{eff}	M_{min}	f_{sat}
Eight-parameter (Contreras et al. 2013)	$1.18^{+0.04}_{-0.06}$	$12.23^{+0.13}_{-0.17}$	$11.18^{+0.09}_{-0.18}$	$0.04^{+0.02}_{-0.04}$
Six-parameter (Contreras et al. 2013)	1.14 ± 0.06	$12.29^{+0.08}_{-0.11}$	$11.03^{+0.17}_{-0.22}$	$0.05^{+0.01}_{-0.02}$
Five-parameter (Contreras et al. 2013/ Geach et al. 2012)	1.15 ± 0.05	$12.20^{+0.08}_{-0.09}$	$11.14^{+0.09}_{-0.12}$	$0.06^{+0.02}_{-0.01}$
Five-parameter (Zheng et al. 2005)	1.24 ± 0.02	$12.44^{+0.06}_{-0.05}$	$11.21^{+0.06}_{-0.05}$	0.04 ± 0.03

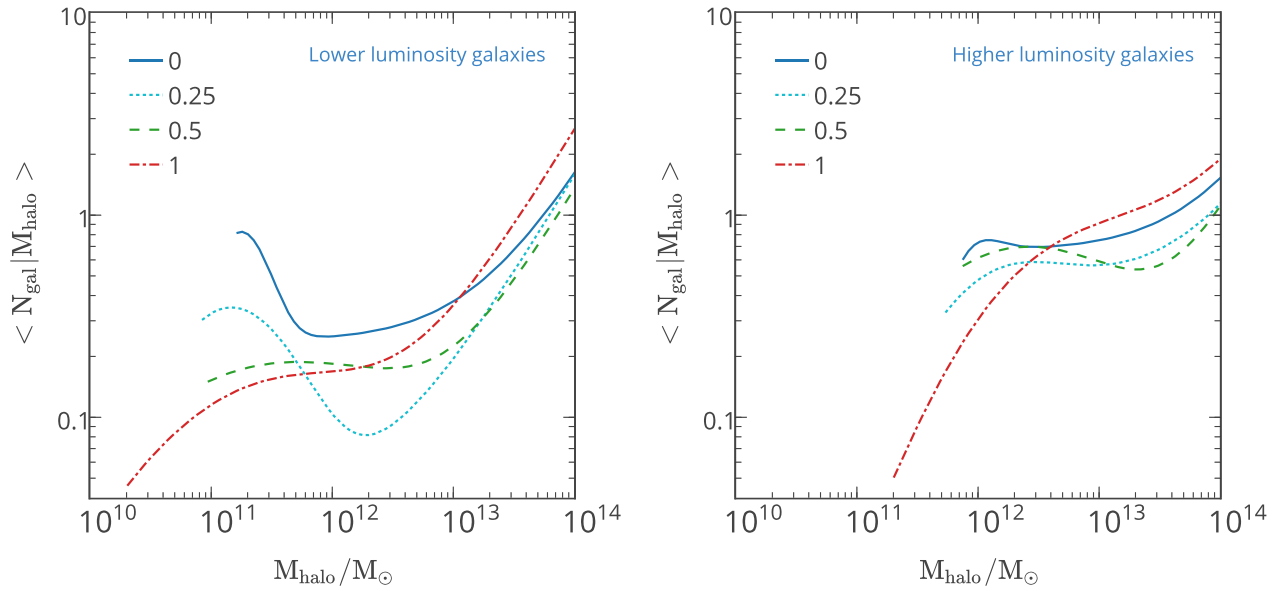

Figure B2. The best-fitting HODs using different lower limits. The left- and right-hand panels show HODs fitted to lower and higher luminosity halves of the sample, respectively. The legends give the lower limit of the integral. For example, 0.5 indicates that we integrate to 0.5 dex below M_{min}. The overall shape of the HOD is strongly dependent on the lower limit. Integrating to lower limits shifts M_{min} to higher values, and leaves it less well constrained.

Table B2. Derived parameters from HOD fits to correlation functions at $z = 0.8$, integrating to different lower limits. Most parameters are unaffected by this lower limit, and the projected two-point correlation functions are near-identical. However, $M_{\rm min}$ moves towards higher values and becomes less well constrained as we integrate to lower halo masses. We therefore adopt $M_{\rm min}$ as the lower limit to our HOD fits, essentially truncating the parametrization described in Section 5.

Fitted HOD parameters for lower luminosity HiZELS emitters at $z \sim 0.8$ ($41.72 < \log_{10}(L_{\rm H\,\alpha}) < 42.07$)					
Lower limit	$b_{\rm eff}$	$\log_{10}(M_{\rm eff}/{\rm M}_\odot)$	$\log_{10}(M_{\rm min}/{\rm M}_\odot)$	σ	$f_{\rm sat}$
$\log_{10}(M_{\rm min}/{\rm M}_\odot)$	$1.05^{+0.05}_{-0.05}$	$11.92^{+0.09}_{-0.06}$	$11.09^{+0.10}_{-0.09}$	$0.3^{+0.2}_{-0.1}$	$0.03^{+0.01}_{-0.01}$
$\log_{10}(M_{\rm min}/{\rm M}_\odot) - 0.25$	$1.03^{+0.05}_{-0.03}$	$11.88^{+0.10}_{-0.08}$	$11.21^{+0.14}_{-0.12}$	$0.3^{+0.3}_{-0.1}$	$0.03^{+0.01}_{-0.01}$
$\log_{10}(M_{\rm min}/{\rm M}_\odot) - 0.5$	$1.03^{+0.05}_{-0.03}$	$11.87^{+0.11}_{-0.08}$	$11.27^{+0.17}_{-0.13}$	$0.5^{+0.3}_{-0.3}$	$0.03^{+0.01}_{-0.01}$
$\log_{10}(M_{\rm min}/{\rm M}_\odot) - 1$	$1.00^{+0.07}_{-0.04}$	$11.85^{+0.13}_{-0.10}$	$11.43^{+0.21}_{-0.19}$	$0.7^{+0.2}_{-0.3}$	$0.02^{+0.01}_{-0.01}$
Fitted HOD parameters for higher luminosity HiZELS emitters at $z \sim 0.8$ [$42.07 < \log_{10}({\rm L_{H\,\alpha}}) < 42.42$]					
Lower limit	$b_{\rm eff}$	$\log_{10}(M_{\rm eff}/{\rm M}_\odot)$	$\log_{10}(M_{\rm min}/{\rm M}_\odot)$	σ	$f_{\rm sat}$
$\log_{10}(M_{\rm min}/{\rm M}_\odot)$	$1.47^{+0.06}_{-0.08}$	$12.54^{+0.08}_{-0.11}$	$11.85^{+0.07}_{-0.10}$	$0.5^{+0.3}_{-0.3}$	$0.02^{+0.01}_{-0.01}$
$\log_{10}(M_{\rm min}/{\rm M}_\odot) - 0.25$	$1.46^{+0.05}_{-0.08}$	$12.52^{+0.08}_{-0.12}$	$12.02^{+0.08}_{-0.10}$	$0.6^{+0.3}_{-0.3}$	$0.02^{+0.01}_{-0.01}$
$\log_{10}(M_{\rm min}/{\rm M}_\odot) - 0.5$	$1.45^{+0.05}_{-0.08}$	$12.51^{+0.07}_{-0.12}$	$12.17^{+0.13}_{-0.16}$	$0.7^{+0.2}_{-0.3}$	$0.02^{+0.01}_{-0.01}$
$\log_{10}(M_{\rm min}/{\rm M}_\odot) - 1$	$1.42^{+0.05}_{-0.06}$	$12.51^{+0.07}_{-0.09}$	$12.45^{+0.21}_{-0.24}$	$0.7^{+0.2}_{-0.3}$	$0.02^{+0.01}_{-0.01}$

with $M_{\rm min}$, with a higher $M_{\rm min}$ and larger σ producing the same correlation function as a lower $M_{\rm min}$ and smaller σ. Derived values of $M_{\rm min}$ are therefore highly dependent on the lower limit of the integral. Table B2 shows the fitted parameters. All other derived values depend little on the choice of integration limit.

For the purposes of this study, we fix the lower limit of the integral to be $M_{\rm min}$. $M_{\rm min}$ is then a more physical quantity: the minimum mass of haloes hosting central galaxies. This is also consistent with parametrizations used by other authors, and enables easier comparison of minimum halo masses.

B3 MCMC fits to correlation functions

In Section 5.3, we described the HOD fitting process. We primarily used the HMF (Murray et al. 2013) and HALOMOD codes (Murray, 2015), which make use of the MCMC fitting software EMCEE (Foreman-Mackey et al. 2013) to derive HOD parameters. In Fig. B3, we show an example of the MCMC output. Whilst the five individual HOD parameters are highly correlated, we can still constrain the derived parameters, $b_{\rm eff}$, $M_{\rm eff}$, $M_{\rm min}$ and $f_{\rm sat}$ and obtain good fits to the correlation functions.

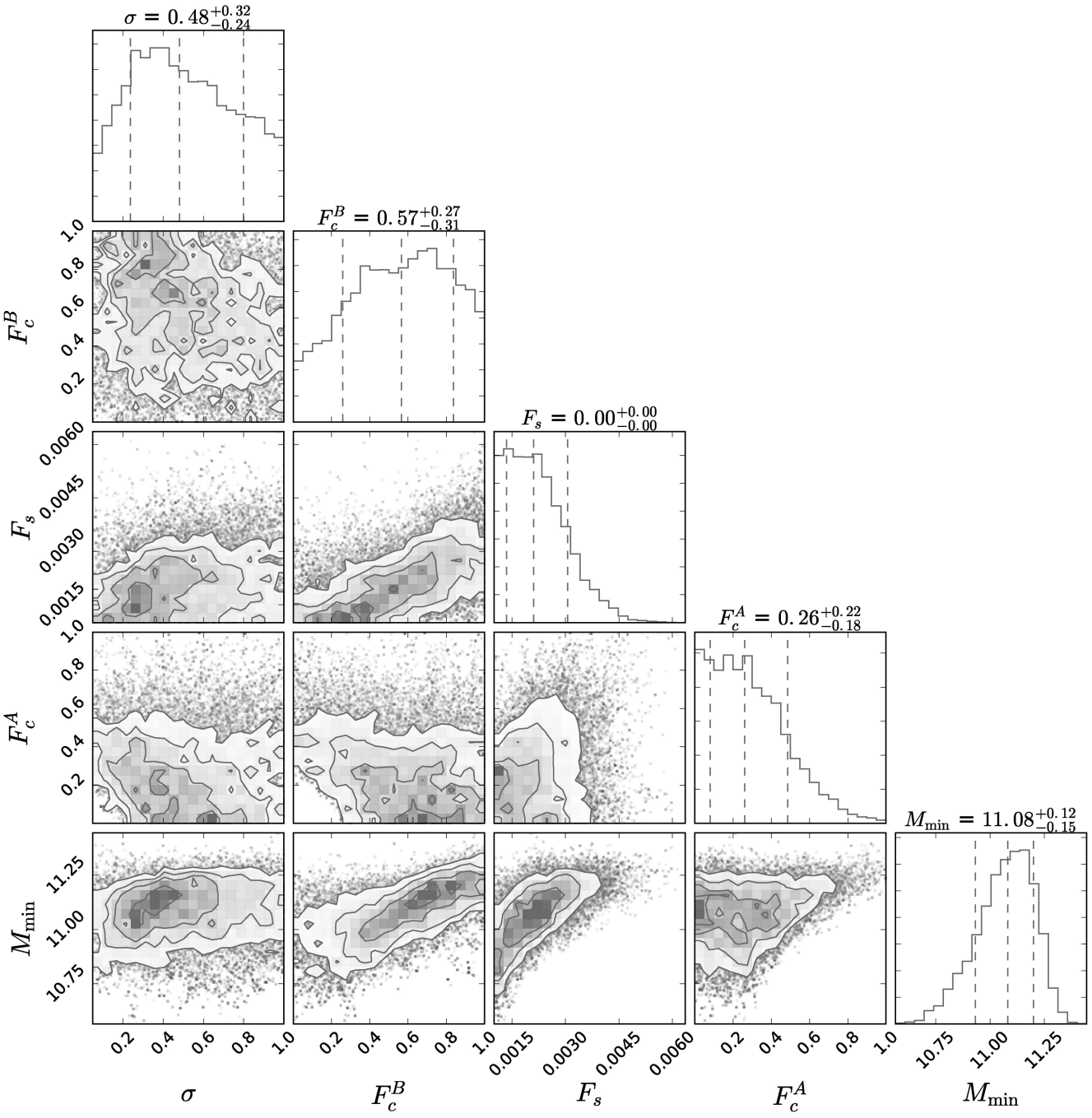

Figure B3. An example of the output from the MCMC HOD fit to the two-point correlation function (Foreman-Mackey 2014), constructed using the 'full' sample of galaxies at $z = 0.8$. The five fitted parameters are highly correlated, but we obtain good constraints on the derived parameters, $b_{\rm eff}$, $M_{\rm eff}$, $M_{\rm min}$ and $f_{\rm sat}$.

This paper has been typeset from a TEX/LATEX file prepared by the author.